

---

# Improved Order Analysis and Design of Exponential Integrator for Diffusion Models Sampling

---

**Qinsheng Zhang**

Georgia Institute of Technology  
qzhang419@gatech.edu

**Jiaming Song**

Luma AI  
jiaming.tsong@gmail.com

**Yongxin Chen**

Georgia Institute of Technology  
yongchen@gatech.edu

## Abstract

Efficient differential equation solvers have significantly reduced the sampling time of diffusion models (DMs) while retaining high sampling quality. Among these solvers, exponential integrators (EI) have gained prominence by demonstrating state-of-the-art performance. However, existing high-order EI-based sampling algorithms rely on degenerate EI solvers, resulting in inferior error bounds and reduced accuracy in contrast to the theoretically anticipated results under optimal settings. This situation makes the sampling quality extremely vulnerable to seemingly innocuous design choices such as timestep schedules. For example, an inefficient timestep scheduler might necessitate twice the number of steps to achieve a quality comparable to that obtained through carefully optimized timesteps. To address this issue, we reevaluate the design of high-order differential solvers for DMs. Through a thorough order analysis, we reveal that the degeneration of existing high-order EI solvers can be attributed to the absence of essential order conditions. By reformulating the differential equations in DMs and capitalizing on the theory of exponential integrators, we propose refined EI solvers that fulfill all the order conditions, which we designate as Refined Exponential Solver (RES). Utilizing these improved solvers, RES exhibits more favorable error bounds theoretically and achieves superior sampling efficiency and stability in practical applications. For instance, a simple switch from the single-step DPM-Solver++ to our order-satisfied RES solver when Number of Function Evaluations (NFE) = 9, results in a reduction of numerical defects by 25.2% and FID improvement of 25.4% (16.77 vs 12.51) on a pre-trained ImageNet diffusion model.

## 1 Introduction

Diffusion models (DMs) [13, 47] have recently garnered significant interest as powerful and expressive generative models. They have demonstrated unprecedented success in text-to-image synthesis [38, 40, 1] and extended their impact to other data modalities, such as 3D objects [34, 26, 43, 3], audio [24], time series [48, 4], and molecules [55, 36, 57]. However, DMs suffer from slow generation due to their iterative noise removal process. Generative adversarial networks (GANs) require only a single network evaluation to generate a batch of images, whereas DMs may necessitate hundreds or thousands of network function evaluations (NFEs) to transform Gaussian noise into clean data.

Recently, a surge of research interest has been directed toward accelerating the sampling process in diffusion models. One strategy involves the distillation of deterministic generation. Despite requiring additional computational resources, this approach can reduce the number of NFEs to fewer than five [41, 45, 33]. Nevertheless, distillation methods often depend on training-free sampling

methods during the learning process and are only applicable to the specific model being distilled, thereby limiting their flexibility compared to training-free sampling methods [32]. Another line of investigation is aimed at designing generic sampling techniques that can be readily applied to any pre-trained DMs. Specifically, these techniques leverage the connection between diffusion models and stochastic differential equations (SDEs), as well as the feasibility of deterministically drawing samples by solving the equivalent Ordinary Differential Equations (ODEs) for marginal probabilities, known as probability flow ODEs [47, 44]. Research in this domain focuses on the design of efficient numerical solvers to expedite the process [29, 59, 30, 60, 21, 31, 61]. Despite the significant empirical acceleration, numerous methods that claim the same order of numerical error convergence rate demonstrate significant disparities in practical application. Furthermore, these approaches often incorporate a range of techniques and designs that may obscure the actual factors contributing to the acceleration, such as various thresholding [9, 40], and sampling time optimization [8, 21]. (See App A for more related works and discussions.)

In this study, we initiate by revisiting different diffusion probability flow ODE parameterizations, underlining the vital role of approximation accuracy for integrals in the ODE solution in various sampling algorithms. This directly impacts both the quality and speed of sampling (Sec 3.1). Through a change-of-variable process, we further unify the ODEs for the noise prediction model and data prediction into a singular, canonical semilinear ODE. We then conduct an exhaustive order analysis for the single-step numerical scheme for the semilinear ODE and contend that the widely accepted sampling algorithm, which is based on the exponential integrator (EI), contravenes order conditions. This leads to inferior error bounds, compromised accuracy, and a lack of robustness compared to the theoretically projected outcomes under optimal settings (Sec 3.2).

In response, we propose Refined Exponential Solver (RES), which offers more favorable error recursion both theoretically and empirically, thus ensuring superior sampling efficiency and robustness (Sec 3.3). Moreover, our single-step scheme can be seamlessly integrated to enhance multistep deterministic (Sec 3.4) and stochastic sampling algorithms (Sec 3.5), surpassing the performance of contemporary alternatives. Lastly, we undertake comprehensive experiments with various diffusion models to demonstrate the generalizability, superior efficiency, and enhanced stability of our approach, in comparison with existing works (Sec 4). In summary, our contributions are as follows:

- We revisit and reevaluate diffusion probability flow ODE parameterizations and reveal the source of approximation error.
- To minimize error, we propose a unified canonical semilinear ODE, identify the overlooked order condition in existing studies, and rectify this oversight.
- We introduce RES, an innovative method that provides improved error recursion, both theoretically and empirically. Extensive experiments are conducted to show its generalizability, superior efficiency, and enhanced stability. For example, it shows up to 40% acceleration by switching single-step DPM-Solver++ to single-step RES under a suboptimal time scheduling.

## 2 Background

Given a data distribution of interest, denoted as  $p_{data}(\mathbf{x})$  where  $\mathbf{x} \in \mathcal{X}$ , a diffusion model consists of a forward noising process that diffuses data point  $\mathbf{x}$  into random noise and a backward denoising process that synthesizes data via removing noise iteratively starting from random noise. We start our discussion with simple variance-exploding diffusion models [46], which can be generalized to other diffusion models under the unifying framework introduced by Karras et al. [21]. Concretely, the forward noising process defines a family of distributions  $p(\mathbf{x}; \sigma(t))$  dependent on time  $t$ , which is obtained by adding *i.i.d.* Gaussian noise of standard deviation  $\sigma(t)$  to noise-free data samples. We choose  $\sigma(t)$  to be monotonically increasing with respect to time  $t$ , such as  $\sigma(t) = t$ .

To draw samples from diffusion models, a backward synthesis process is required to solve the following stochastic differential equation (SDE) [58, 19, 21], starting from  $\mathbf{x}(T) \sim \mathcal{N}(\mathbf{0}, \sigma(T)^2 \mathbf{I})$  for a large enough  $T$ :

$$d\mathbf{x} = - \underbrace{\dot{\sigma}(t)\sigma(t)\nabla_{\mathbf{x}} \log p(\mathbf{x}; \sigma(t))dt}_{\text{Probabilistic ODE}} - \underbrace{\beta_t\sigma(t)^2\nabla_{\mathbf{x}} \log p(\mathbf{x}; \sigma(t))dt + \sqrt{2\beta_t}\sigma(t)d\omega_t}_{\text{Langevin process}}, \quad (1)$$

where  $\nabla_{\mathbf{x}} \log p(\mathbf{x}; \sigma(t))$  is the score function (*i.e.*, gradient of log-probability),  $\omega_t$  is the standard Wiener process, and  $\beta_t$  is a hyperparameter that controls the stochasticity of the process. Eq (1) reduces

**Table 1:** Different parametrizations of the probabilistic ODE.

Parametrization	Location	Velocity	Time	Semi-linear
EDM / DEIS	$\mathbf{x}$	$(\mathbf{x} - D_\theta(\mathbf{x}, t))/t$	$t := \sigma$	No
logSNR	$\mathbf{x}$	$-\mathbf{x} + D_\theta(\mathbf{x}, e^{-\lambda_D})$	$\lambda_D := -\log \sigma$	Yes
Negative logSNR	$\mathbf{y} := \mathbf{x}/e^{\lambda_\epsilon}$	$-\mathbf{y} + \epsilon_\theta(e^{\lambda_\epsilon} \mathbf{y}, e^{\lambda_\epsilon})$	$\lambda_\epsilon := \log \sigma$	Yes

to deterministic probabilistic flow ODE [47] when  $\beta = 0$ . Some popular methods, such as variance-preserving diffusion models, introduce an additional scale schedule  $s(t)$  and consider  $\mathbf{x} = s(t)\hat{\mathbf{x}}$  to be a scaled version of the original, non-scaled data  $\hat{\mathbf{x}}$ . Though the introduction of scale schedule  $s(t)$  will result in a different backward process, we can undo the scaling and reduce their sampling SDEs to Eq (1). Note that we focus on non-scaling diffusion models in this paper for simplicity and leave the extension to other diffusion models in App B. The score function  $\nabla_{\mathbf{x}} \log p(\mathbf{x}; \sigma(t))$  of noised data distribution at a particular noise level  $\sigma$  can be learned via a denoising score matching objective [51]:

$$L_\sigma(\theta) = \mathbb{E}_{\mathbf{x} \sim p_{data}, \epsilon \sim \mathcal{N}(0, \mathbf{I})} [\|D_\theta(\mathbf{x} + \sigma\epsilon, \sigma) - \mathbf{x}\|_2^2], \quad (2)$$

where  $D_\theta : \mathcal{X} \times \mathcal{R} \rightarrow \mathcal{X}$  is a time-conditioned neural network that tries to denoise the noisy sample. In the ideal case, having the perfect denoiser  $D_\theta$  is equivalent to having the score function thanks to Tweedie’s formula [11]:

$$D_\theta(\mathbf{x}, \sigma) = \mathbf{x} + \sigma^2 \nabla_{\mathbf{x}} \log p(\mathbf{x}; \sigma). \quad (3)$$

For convenience, we also introduce the noise prediction model, which tries to predict  $\epsilon$  in Eq (2):

$$\epsilon_\theta(\mathbf{x}, \sigma) := \frac{\mathbf{x} - D_\theta(\mathbf{x}, \sigma)}{\sigma}. \quad (4)$$

### 3 Refined exponential solver RES

Even with the same trained diffusion model, different solvers of Eq (1) will lead to samplers of drastically different efficiency and quality. In this section, we present a unified formulation to the various probability flow ODE being considered (Sec 3.1), analyze the numerical approximation errors for general single-step methods (Sec 3.2), and find the optimal set of coefficients that satisfies the desired order conditions and minimizes numerical error (Sec 3.3). We then extend the improvement to the stochastic setting (Sec 3.4) and multistep sampling methods (Sec 3.5).

#### 3.1 Better parameterizations for probability flow ODE

The probability flow ODE in diffusion models in Eq (1) is first order, and thus we can draw some analogies between  $\mathbf{x}$  and “location”,  $t$  and “time”, and  $-\dot{\sigma}(t)\sigma(t)\nabla_{\mathbf{x}} \log p(\mathbf{x}, \sigma(t))$  as “velocity”. In general, an ODE is easier to solve if the “velocity” term has smaller first-order derivatives [35, 28]. Here, we list several different parameterizations for these quantities. While the exact solutions to these ODEs are the same, the numerical solutions can differ dramatically.

**EDM** In EDM [21], the location term is on the data space  $\mathbf{x}$ , the probability flow ODE in Eq (1) with  $\beta_t = 0$  simplifies to the following equation:

$$d\mathbf{x} = \frac{\mathbf{x} - D_\theta(\mathbf{x}, \sigma(t))}{\sigma(t)} \dot{\sigma}(t) dt. \quad (5)$$

To solve Eq (5), Karras et al. [21] interpret the term  $\frac{\mathbf{x} - D_\theta(\mathbf{x}, \sigma(t))}{\sigma(t)} \dot{\sigma}(t)$  as a black box function and choose  $\sigma(t) = t$ , and then apply a standard second-order Heun ODE solver.

**DEIS** Similarly, DEIS [59] uses the noise prediction model  $\epsilon_\theta$  to parametrize the ODE:

$$d\mathbf{x} = \epsilon_\theta(\mathbf{x}, \sigma) d\sigma. \quad (6)$$

It is not hard to see that this is equivalent to the EDM one if we set  $\sigma$  to  $t$ .

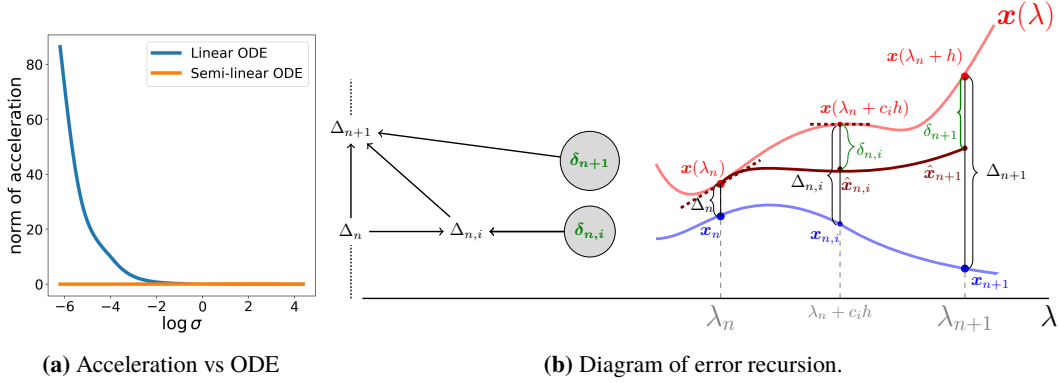


**Figure 1:** Fig 1a. Along the trajectory of an exact solution to the probability flow ODE, semi-linear ODE with logarithm transformation parametrization on noise level  $\sigma$  has smaller “acceleration”, *i.e.*, the time-derivative of “velocity”. The curves are averaged over 512 solutions on the pre-trained ImageNet model [21]. This suggests that semi-linear ODE incur less discretization error when solving ODEs. Fig 1b. The auxiliary trajectory  $\hat{\mathbf{x}}$  starts from exact solution  $\mathbf{x}$  and is built upon numerical integration proposed in Eq (11). The diagram depicts that numerical defects  $\Delta_{n+1}$  between  $\mathbf{x}(\lambda_{n+1})$  and numerical solution  $\mathbf{x}_{n+1}$  is a result of accumulated intermediate defects  $\{\delta_n, \delta_{n,i}\}$  in each step, which is the discrepancy between the auxiliary trajectory and the exact solution trajectory.

**logSNR** We explore an alternative probability flow ODE parameterization based on the denoising model  $D_\theta$ . We consider  $\lambda_D(t) := -\log \sigma(t)$ , which can be treated as the log signal-to-noise ratio (logSNR, [22]) between coefficients of the signal  $\mathbf{x}(0)$  and noise  $\epsilon$ . With  $d\lambda_D(t) = \frac{-\dot{\sigma}(t)}{\sigma(t)} dt$ , Eq (5) can be reformulated as follows:

$$\frac{d\mathbf{x}}{d\lambda_D} = -\mathbf{x} + g_D(\mathbf{x}, \lambda_D), \quad g_D(\mathbf{x}, \lambda_D) := D_\theta(\mathbf{x}, e^{-\lambda_D}). \quad (7)$$

**Negative logSNR** Alternatively, we can restructure Eq (6) by employing a change-of-variables approach with  $\mathbf{y}(t) := \frac{\mathbf{x}(t)}{\sigma(t)}$ ,  $\lambda_\epsilon(t) := \log \sigma(t)$  for the noise prediction model  $\epsilon_\theta$ :

$$\frac{d\mathbf{y}}{d\lambda_\epsilon} = -\mathbf{y} + g_\epsilon(\mathbf{y}, \lambda_\epsilon), \quad g_\epsilon(\mathbf{y}, \lambda_\epsilon) := \epsilon_\theta(e^{\lambda_\epsilon} \mathbf{y}, e_\epsilon^\lambda), \quad (8)$$

where  $\lambda_\epsilon$  is the negative logSNR. We observe that Eq (7) and (8) possess highly similar ODE structures. In fact, they are both *semilinear parabolic problems* in the numerical analysis literature [16], *i.e.*, the velocity term is a linear function of location plus a non-linear function of location ( $g_D$  or  $g_\epsilon$ ). This suggests that ODEs with either epsilon prediction or data prediction models can be addressed within a *unified* framework. We summarize these different parametrizations in Tab 1.

A notable advantage of the logSNR and negative SNR parametrizations is that their velocity terms along exact solution trajectory, such as  $-\mathbf{x}(\lambda_D) + g_D(\mathbf{x}(\lambda_D), \lambda_D)$ , are smoother than the velocity term in the ODE for EDM/DEIS. We illustrate this in Fig 1a, which shows that the norm of the derivative of the EDM velocity term grows rapidly as  $\sigma \rightarrow 0$ ; this may explain why the timestep scheduling used in popular samplers (such as DDIM and EDM) often place more steps at lower noise levels.

For the rest of the section, we focus on logSNR (Eq (7)); theoretical conclusions and practical algorithms can be easily transferred to negative logSNR (Eq (8)). For notational simplicity, we substitute  $\lambda$  for  $\lambda_D$  and  $g$  for  $g_D$ , so our ODE in Eq (7) becomes:

$$\frac{d\mathbf{x}}{d\lambda} = -\mathbf{x} + g(\mathbf{x}, \lambda), \quad (9)$$

Suppose that our ODE solver advances for a step size of  $h$  from  $\mathbf{x}(\lambda)$ , then the exact solution  $\mathbf{x}(\lambda + h)$  to this ODE, as given by the *variation-of-constants* formula, is represented as follows:

$$\mathbf{x}(\lambda + h) = e^{-h} \mathbf{x}(\lambda) + \int_0^h e^{(\tau-h)} g(\mathbf{x}(\lambda + \tau), \lambda + \tau) d\tau. \quad (10)$$

However, the computation of this exact solution confronts two significant challenges: the intractability of the integral and the inaccessible integrand, which involves the evaluation of the denoiser on the exact solution  $\mathbf{x}(\lambda + \tau)$ . To approximate the intractable integration in Eq (10), we start with the single-step approach and derive its order conditions.

### 3.2 Single-step numerical schemes and defect analysis

To approximate the exact solution in Eq (10), the numerical scheme of explicit single-step methods, characterized by  $s$ -stages, can be described as follows:

$$\mathbf{x}_{n+1} = e^{-h_n} \mathbf{x}_n + h_n \sum_{i=1}^s b_i(-h_n) \mathbf{d}_{n,i}, \quad (11a)$$

$$\mathbf{x}_{n,i} = e^{-c_i h_n} \mathbf{x}_n + h_n \sum_{j=1}^{i-1} a_{ij}(-h_n) \mathbf{d}_{n,j}, \quad \mathbf{d}_{n,i} := g(\mathbf{x}_{n,i}, \lambda_n + c_i h_n), \quad (11b)$$

where  $h_n := \lambda_{n+1} - \lambda_n$  denotes the step size from state  $\mathbf{x}_n$  to  $\mathbf{x}_{n+1}$ ,  $\mathbf{x}_{n,i}$  denotes the numerical solution at the  $i$ -th stage with timestep  $\lambda_n + c_i h_n$ , and  $\mathbf{d}_{n,i}$  is the function evaluation at the  $i$ -th stage. Notably,  $\mathbf{x}_n$  denotes the numerical solution at time  $\lambda_n$ , which deviates from the exact solution  $\mathbf{x}(\lambda_n)$ ; similarly, the numerical solution  $\mathbf{x}_{n,i}$  at stage  $i$  deviates from the exact  $\mathbf{x}(\lambda_n + c_i h_n)$ . The coefficients  $a_{ij}, b_i, c_j$  in Eq (11) can be compactly represented using Butcher tableaux Tab 2 [35].

**Table 2:** *Left:* Tableau form of  $\{a_{ij}, b_i, c_j\}$  for numerical scheme in Eq (11). For all  $1 \leq j \leq i \leq s$ ,  $a_{ij} = 0$ . *Middle:* For Euler method,  $c_1 = 0, b_1 = 1$ . *Right:* For Heun's method,  $c_1 = 0, c_2 = 1, a_{21} = 1, b_1 = b_2 = 0.5$ . Unlike our RES exponential integrator, the explicit Euler and Heun solvers do not have the additional exponential coefficients (e.g.,  $e^{-h_n}$ ) in front of  $\mathbf{x}_n$  (see Eq (11)). These coefficients are not reflected in the Butcher tableau.

$c_1$					
$c_2$	$a_{21}$			0	
$\vdots$	$\vdots$	$\ddots$			
$c_s$	$a_{s1}$	$\cdots$	$a_{s,s-1}$		
	$b_1$	$\cdots$	$b_{s-1}$		$b_s$

0	1
1	0.5
	0.5

To bound the numerical defect  $\mathbf{x}_n - \mathbf{x}(\lambda_n)$ , we first decompose it into the summation of,  $\mathbf{x}_n - \hat{\mathbf{x}}_n$  and  $\hat{\mathbf{x}}_n - \mathbf{x}(\lambda_n)$ . Here, the auxiliary trajectory  $\hat{\mathbf{x}}_n$  is obtained by substituting  $\mathbf{d}_{n,i}$  in Eq (11) with  $f(\lambda) := g(\mathbf{x}(\lambda), \lambda)$ . Specifically, we define *intermediate numerical defects*  $\delta_n, \delta_{n,i}$  as

$$\delta_{n,i} := \mathbf{x}(\lambda_n + c_i h_n) - \hat{\mathbf{x}}_{n,i}, \quad \hat{\mathbf{x}}_{n,i} = e^{-c_i h_n} \mathbf{x}(\lambda_n) - h_n \sum_{j=1}^{i-1} a_{ij}(-h_n) f(\lambda_n + c_j h_n), \quad (12a)$$

$$\delta_{n+1} := \mathbf{x}(\lambda_{n+1}) - \hat{\mathbf{x}}_{n+1}, \quad \hat{\mathbf{x}}_{n+1} = e^{-h_n} \mathbf{x}(\lambda_n) - h_n \sum_{i=1}^s b_i(-h_n) f(\lambda_n + c_i h_n). \quad (12b)$$

Intuitively, defects  $\delta_{n,i}, \delta_{n+1}$  are caused by approximating the intractable integration in Eq (10) by finite summation in Eq (11). Let  $\Delta_n := \mathbf{x}_n - \mathbf{x}(\lambda_n)$ ,  $\Delta_{n,i} := \mathbf{x}_{n,i} - \mathbf{x}(\lambda_n + c_i h_n)$ , we can derive error recursion with the help of  $\delta_{n,i}, \delta_{n+1}$ , such that

$$\Delta_{n+1} = e^{-h_n} \Delta_n + h \sum_{i=1}^s b_i(-h_n) (g(\mathbf{x}_{n,i}, \lambda_n + c_i h_n) - f(\lambda_n + c_i h_n)) - \delta_{n+1}, \quad (13a)$$

$$\Delta_{n,i} = e^{-c_i h_n} \Delta_n + h \sum_{j=1}^{i-1} a_{ij}(-h_n) (g(\mathbf{x}_{n,j}, \lambda_n + c_j h_n) - f(\lambda_n + c_j h_n)) - \delta_{n,i}. \quad (13b)$$

Eq (13) reveals that numerical defects  $\Delta_{n+1}, \Delta_{n,i}$  are influenced by the emergent intermediate defects  $\delta_{n+1}, \delta_{n,i}$  and defects  $\Delta_n$ , which are themselves modulated by previous intermediate defects. Moreover, the discrepancy  $g(\mathbf{x}_{n,i}, \lambda_n + c_i h_n) - f(\lambda_n + c_i h_n)$  is contingent upon  $\Delta_{n,i}$ . As error recursion illustrated in Fig 1b, the origin of final numerical defects lies in the defects  $\delta_{n+1}, \delta_{n,i}$  in each step. Consequently, to curtail the ultimate defect, it becomes paramount to constrain  $\delta_{n+1}, \delta_{n,i}$ . To establish bounds for  $\Delta_n$  using the above error recursion, the following lemma provides an expansion of intermediate defects, uncovering the association between  $\delta_{n+1}, \delta_{n,i}$  and the derivative of  $f(\lambda)$ .

**Lemma 1.** *Let  $\phi_j(-h_n) = \frac{1}{h_n^j} \int_0^{h_n} e^{\tau-h_n} \frac{\tau^{j-1}}{(j-1)!} d\tau$ , the order- $q$  Taylor expansion of the intermediate defects  $\delta_{n,i}, \delta_{n+1}$  can be formulated as follows:*

$$\delta_{n,i} = \sum_{j=1}^q h_n^j \psi_{j,i}(-h_n) f^{(j-1)}(\lambda_n) + \mathcal{O}(h_n^q) \quad \delta_{n+1} = \sum_{j=1}^q h_n^j \psi_j(-h_n) f^{(j-1)}(\lambda_n) + \mathcal{O}(h_n^q), \quad (14)$$

---

**Algorithm 1** RES Second order Single Update Step with  $c_2$ 


---

```

1: procedure SINGLEUPDATESTEP( $\mathbf{x}_i, \sigma_i, \sigma_{i+1}$ )
2:    $\lambda_{i+1}, \lambda_i \leftarrow -\log(\sigma_{i+1}), -\log(\sigma_i)$ 
3:    $h \leftarrow \lambda_{i+1} - \lambda_i$  ▷ Step length
4:    $a_{21}, b_1, b_2 \leftarrow$  Tab 3 with  $c_2$  ▷ Runge Kutta coefficients
5:    $(\mathbf{x}_{i,2}, \lambda_{i,2}) \leftarrow (e^{-c_2 h} \mathbf{x}_i + a_{21} h D_\theta(\mathbf{x}_i, \lambda_i), \lambda_i + c_2 h)$  ▷ Additional evaluation point
6:    $\mathbf{x}_{i+1} \leftarrow e^{-h} \mathbf{x}_i + h(b_1 D_\theta(\mathbf{x}_i, \lambda_i) + b_2 D_\theta(\mathbf{x}_{i,2}, \lambda_{i,2}))$ 
7:   return  $\mathbf{x}_{i+1}$ 

```

---

where function  $\psi_{j,i}, \psi_j$  for the coefficients of the  $(j-1)$ -th order derivative of  $f(\lambda_n)$  are defined as

$$\psi_{j,i}(-h_n) = \phi_j(-c_i h_n) c_i^j - \sum_{k=1}^{i-1} a_{ik}(-h_n) \frac{c_k^{j-1}}{(j-1)!}, \quad \psi_j(-h_n) = \phi_j(-h_n) - \sum_{k=1}^s b_k(-h_n) \frac{c_k^{j-1}}{(j-1)!}.$$

[Lemma 1](#) furnishes an expansion expression for  $\delta_{n,i}, \delta_{n+1}$ , with each term contingent upon the derivative of  $f$  and coefficients  $\{\psi_j, \psi_{j,i}\}$ . This implies that to minimize numerical defects ( $\Delta_{n+1}$ ), an ODE parameterization that ensures the smoothest possible nonlinear function along the exact solution trajectory should be selected, thus substantiating our choice of the logarithmic transformation on the noise level. To this end, we can constrain numerical defects  $\delta_{n+1}, \delta_{n,i}$  by minimizing the magnitude of  $\{\psi_j, \psi_{j,i}\}$ , forming the foundation of the order conditions for the single-step scheme.

### 3.3 Order conditions

With [Eq \(13\)](#) and [Lemma 1](#), we can deduce the conditions necessary to achieve a numerical scheme of order  $q$ . We start with the case of a single-stage solver of order one.

**Theorem 1** (Error bound for solvers that satisfy the 1st-order condition). *When  $\psi_1(-h_i) = 0$  is satisfied for  $1 \leq i \leq n$ , the error bound of first-order solver based on [Eq \(11\)](#)*

$$\|\mathbf{x}_n - \mathbf{x}(\lambda_n)\| \leq Ch \sup_{\lambda_{\min} \leq \lambda \leq \lambda_{\max}} \|f'(\lambda)\| \quad (15)$$

holds for  $h = \max_{1 \leq i \leq n} h_i$ . The constant  $C$  is independent of  $n, h$ .

With [Thm 1](#),  $b_1(-h) = \phi_1(-h)$  and the numerical scheme reads

$$\mathbf{x}_{n+1} = e^{-h_n} \mathbf{x}_n + h_n \phi_1(-h) g(\mathbf{x}_n, \lambda_n), \quad (16)$$

which is known as exponential Euler [16] or DDIM for diffusion model [44]. Although our order analysis aligns with existing work [30, 59], the distinction emerges in high-order methods.

**Theorem 2** (Error bound for solvers that satisfy the 1st- and 2nd-order conditions). *When  $\psi_1(-h_i) = \psi_2(-h_i) = \psi_{1,2}(-h_i) = 0$  is satisfied for  $1 \leq i \leq n$ , the error bound of second order solver based on [Eq \(11\)](#)*

$$\|\mathbf{x}_n - \mathbf{x}(\lambda_n)\| \leq Ch^2 \left( \sup_{\lambda_{\min} \leq \lambda \leq \lambda_{\max}} \|f'(\lambda)\| + \sup_{\lambda_{\min} \leq \lambda \leq \lambda_{\max}} \|f''(\lambda)\| \right) \quad (17)$$

holds for  $h = \max_{1 \leq i \leq n} h_i$ . The constant  $C$  is independent of  $n, h$ .

To satisfy order conditions in [Thm 2](#), the optimal Butcher tableau can be parameterized by  $c_2$  as shown in [Tab 3](#). It turns out the single-step scheme proposed in DPM-Solver++ [31] can also be reformulated with a different Butcher tableau as shown in [Tab 3](#) (See [App B](#)). Nevertheless, compared with [Thm 2](#), DPM-Solver++ breaks the order condition  $\psi_2(-h) = 0$ . Therefore, DPM-Solver++ does not fully satisfy the full order condition and introduces additional errors in solving ODEs (See [App B](#)) theoretically. Practically, we find our numerical scheme that obeys the order conditions admits smaller numerical defects and generates higher sample quality from diffusion models. Single-step schemes for orders higher than 3 can also be derived, but we leave them for future work.

**Proposition 1** ((Informal)). *Employing the Butcher tableau outlined in [Tab 3](#), the single-step method [Eq \(11\)](#), characterized by three stages, functions as a third-order solver.*

**Table 3:** Butcher tableau comparison between RES and DPM-Solver++ [31] for step size  $h$ , where  $\phi_i := \phi_i(-h)$  is defined in Lemma 1, and we further define  $\phi_{i,j} := \phi_{i,j}(-h) = \phi_i(-c_j h)$ . †:  $\gamma$  in third order RES needs to satisfy  $2(\gamma c_2 + c_3) = 3(\gamma c_2^2 + c_3^3)$ . The second order tableau is completely characterized by  $c_2$ , whereas the third order is parameterized by both  $c_2$  and  $c_3$ .

	Second Order	Third Order†	Order conditions
RES	$\begin{array}{c cc} 0 & & \\ c_2 & c_2\phi_{1,2} & \\ \hline 0 & \phi_1 - \frac{1}{c_2}\phi_2 & \frac{1}{c_2}\phi_2 \end{array}$	$\begin{array}{c ccc} 0 & & & \\ c_2 & c_2\phi_{1,2} & & \\ c_3 & c_3\phi_{1,3} - a_{32} & \gamma c_2\phi_{2,2} + \frac{c_2^2}{c_3}\phi_{2,3} & \\ \hline & \phi_1 - b_2 - b_3 & \frac{\gamma}{\gamma c_2 + c_3}\phi_2 & \frac{1}{\gamma c_2 + c_3}\phi_2 \end{array}$	Yes
DPM Solver++	$\begin{array}{c cc} 0 & & \\ c_2 & c_2\phi_{1,2} & \\ \hline 0 & (1 - \frac{1}{2c_2})\phi_1 & \frac{1}{2c_2}\phi_1 \end{array}$	$\begin{array}{c ccc} 0 & & & \\ c_2 & c_2\phi_{1,2} & & \\ c_3 & c_3\phi_{1,3} - a_{32} & \frac{c_2^2}{c_3}\phi_{2,3} & \\ \hline & \phi_1 - b_2 - b_3 & 0 & \frac{1}{c_3}\phi_2 \end{array}$	Degenerate

### Algorithm 2 RES Single-Step Sampler

```

1: procedure SINGLESAMPLER( $D_\theta, \sigma_{i \in \{0, \dots, N\}}, \eta_{i \in \{0, \dots, N\}}$ )
2:   sample  $\mathbf{x}_0 \sim \mathcal{N}(\mathbf{0}, \sigma_0^2 \mathbf{I})$  ▷ Generate initial sample at  $\sigma_0$ 
3:   for  $i \in \{0, \dots, N - 1\}$  do
4:     sample  $\epsilon_i \sim \mathcal{N}(\mathbf{0}, \mathbf{I})$ 
5:      $\bar{\sigma}_i \leftarrow \sigma_i + \eta_i \sigma_i$ 
6:      $\bar{\mathbf{x}}_i \leftarrow \mathbf{x}_i + \sqrt{\bar{\sigma}_i^2 - \sigma_i^2} \epsilon_i$  ▷ Move from  $\sigma_i$  to  $\bar{\sigma}_i$  via adding noise
7:      $\mathbf{x}_{i+1} \leftarrow \text{SingleUpdateStep}(\bar{\mathbf{x}}_i, \bar{\sigma}_i, \sigma_{i+1})$  ▷ Run single update step from  $\bar{\sigma}_i$  to  $\sigma_{i+1}$ 
8:   return  $\mathbf{x}_N$  ▷ Return noise-free sample at  $t_N$ 

```

### 3.4 Single-step update for deterministic and stochastic sampler

With the single-step update scheme developed in Sec 3.3, we are prepared to develop a deterministic sampling algorithm by iteratively applying Eq (11) with the corresponding Butcher tableau. Inspired by the stochastic samplers proposed in Karras et al. [21], which alternately execute a denoising backward step and a diffusion forward step, we can replace the original Heun-based single-step update with our improved single-step method. Concretely, one update step of our stochastic sampler consists of two substeps. The first substep simulates a forward noising scheme with a relatively small step size, while the subsequent substep executes a single-step ODE update with a larger step. We unify both samplers in Alg 2 where the hyperparameter  $\eta$  determines the degree of stochasticity.

### 3.5 Multi-step scheme

Instead of constructing a single-step multi-stage numerical scheme to approximate the intractable integration in Eq (10), we can employ a multi-step scheme that capitalizes on the function evaluations from previous steps. Analogous to the analysis in Sec 3.2 and conclusions in Thm 2, we can extend these results to a multi-step scheme, the details of which are provided in App D. Intuitively, multi-step approaches implement an update similar to Eq (11a). Instead of selecting intermediate states and incurring additional function evaluations, a multi-step method reuses function evaluation output from previous steps. In this work, our primary focus is on the multi-step predictor case. However, our framework and analysis can also be applied to derive multi-step corrector, which has been empirically proven to further improve sampling quality [61, 25].

## 4 Experiments

We further extend our experiments to address the following queries: (1) Do the deterministic numerical schemes of RES outperform existing methods in terms of reduced numerical defects and enhanced robustness? (2) Does a reduction in numerical defects translate to improved sampling quality? (3) Can our single-step numerical scheme enhance the performance of existing stochastic samplers? (4) How does RES perform across various unguided and guided diffusion models?

**Numerical defects for deterministic sampler** First, we investigate the evolution of numerical defects  $\|\mathbf{x}_N - \mathbf{x}(0)\|$  in  $L1$  norm as the number of function evaluations (NFE) increases in pre-trained ImageNet diffusion models with default hyperparameters. Since the exact solution  $\mathbf{x}(0)$  is unavailable, we approximate it using a 500-step RK4 solution, which exhibits negligible changes

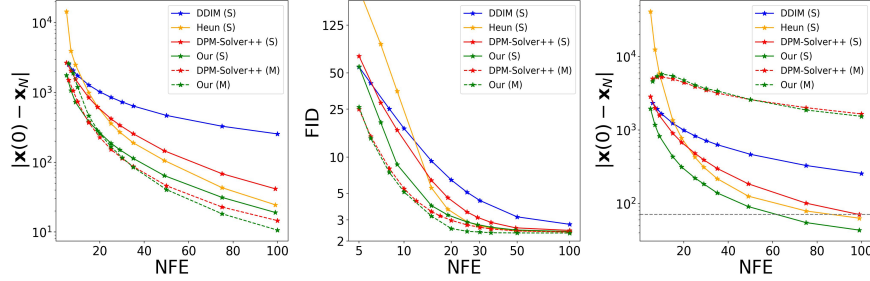


**Figure 2:** Comparison among various deterministic samplers on pretrained ImageNet diffusion model [21]. (S) indicates single-step methods while (M) for multistep methods. (Left) Numerical defects of various sampling algorithms vs the number of function evaluation (NFE) with recommended time scheduling [21]. (Middle) FID of various sampling algorithms vs NFE with recommended time scheduling. (Right) Numerical defects vs NFE with suboptimal time schedule. RES (S) shows better robustness against suboptimal-scheduling. Remarkably, with only 59 NFE, the single-step RES attains a numerical accuracy on par with the 99 NFE DPM-Solver++ (S).

with additional steps. For a fair comparison, we evaluate the **second-order** RES against single-step DPM-Solver++(S)[31] and Heun [21], both claimed to be second-order solvers. We also include first order DDIM [44] as a baseline. Our findings indicate that single-step RES exhibits significantly smaller numerical defects, consistent with our theoretical analysis. RES based on the noise prediction model (negative logSNR) surpasses the data prediction model (logSNR) in performance for guidance-free diffusion models; we provide a detailed presentation of the former here (More details in App E). Additionally, we compare single-step solvers with multistep solvers, specifically including second-order multistep RES and DPM-Solver++ (M). We observe RES-AB consistently outperforms DPM-Solver++ (M) and both lead to smaller defects compared with single-step methods. We observe that multistep solvers initially reduce numerical defects quickly but display smaller reductions for larger NFE values. We hypothesize that multistep solvers benefit from twice the number of steps compared to single-step methods when the NFE is relatively small.

**Numerical defects and FID** We further investigate the relationship between numerical defects and image sampling quality, using the Frechet Inception Distance (FID) [12]. As shown in Fig 2, smaller numerical defects generally lead to better FID scores as the number of function evaluations (NFE) increases for all algorithms. However, we also observe that the correlation may not be strictly positive and similar defects may lead to different FIDs. We observed a Pearson correlation coefficient of 0.956 between these two metrics, which suggests that better FID scores are *strongly correlated* with smaller numerical defects. Notably, when  $NFE = 9$ , compared with single-step DPM-Solver++, the single step RES with noise prediction model (negative logSNR) reduce 52.75% numerical defects, and 48.3% improvement in FID (16.77 vs 8.66). For RES with data prediction model (logSNR), RES achieves 25.2% numerical defects and 25.4% FID improvement (16.77 vs 12.51).

**Time-scheduling robustness** We also evaluate the performance of these solvers concerning varying timestep schedules. We observe that existing methods lack systematic strategies for optimal timestep selection, often relying on heuristic choices or extensive hyperparameter tuning. An ideal algorithm should demonstrate insensitivity to various scheduling approaches. Instead of using the recommended setting in EDM [21], we test these algorithms under a suboptimal choice with uniform step in  $\sigma$ . While all algorithms exhibit decreased performance under this setting, the single-step RES method outperforms the rest. Notably, single-step methods surpass multi-step methods in this scenario, which signifies the robustness of single-step RES and underscores the benefits of our principled single-step numerical scheme. Besides, to achieve a numerical accuracy comparable to that of the 99 NFE DPM-Solver++ (S), our single-step method requires only 59 NFE.

**Classifier-guided DMs** We further investigate RES diffusion models trained using different schemes, including DDPM-like diffusion models with classifier-based guidance [9]. It is important to note that we employ dynamic thresholding [40] for all experiments to help alleviate pixel over-saturation issues. To ensure a fair comparison, all algorithms differ solely in their numerical update schemes. As depicted in Fig 3, our previous observations remain valid for guided diffusion models trained with different techniques, and RES converges faster than baselines.

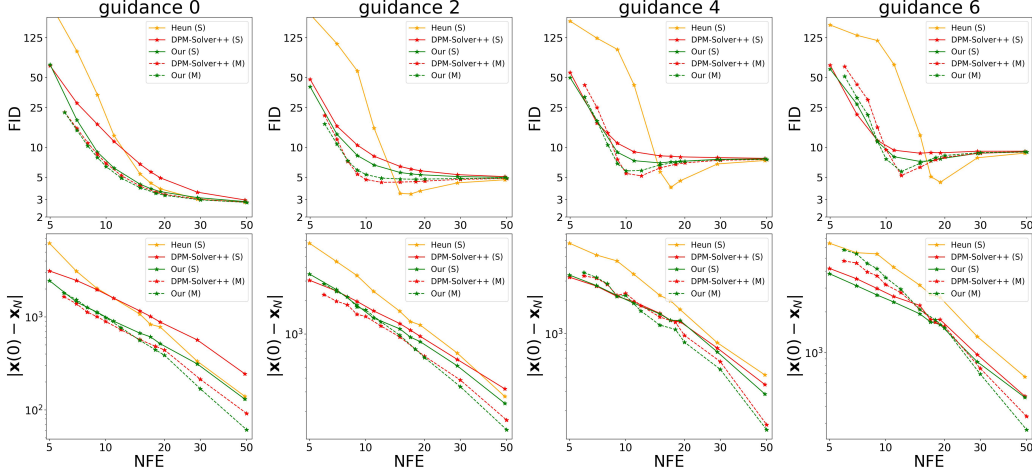


Figure 3: Comparison on DDPM-like classifier-guided diffusion models [9] with different guidance.

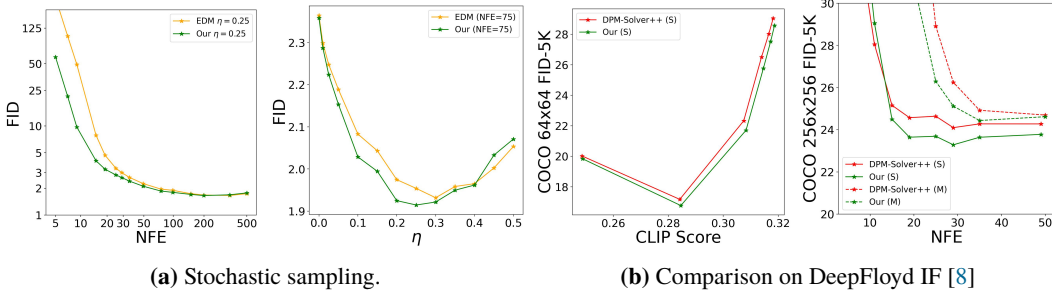


Figure 4: Our efficient single-step method can improve stochastic sampling as shown in Fig 4a. RES outperforms DPM-Solver++ in pixel space text-to-image diffusion models.

**Stochastic sampling with improved single-step algorithm** Existing works demonstrate that stochastic sampling can generate better quality results but demands significantly more computational resources. For example, EDM [21] requires 511 NFEs. Encouraged by the improvement of single-step sampling, we conduct experiments to show that this enhancement can boost stochastic samplers and achieve a favorable trade-off between sampling quality and speed. First, we investigate how FID is affected by NFE for a given  $\eta$ . Next, we sweep different values of  $\eta$  under the same NFE. As illustrated in Fig 4a, we can accelerate the stochastic sampler compared with Heun-based EDM sampler [21].

**Cascaded text-to-image model** Finally, we test our sampling algorithm on cascaded text-to-image models based on DeepFloyd IF diffusion models [8]. We initially evaluate various sampling algorithms for  $64 \times 64$  tasks. We examine how image quality changes with an increasing number of NFEs in Fig 4b. Furthermore, we compare the FID-CLIP score trade-off curves for various classifier-free guidance schemes under the same computational budget. Next, we incorporate a super-resolution diffusion model conditioned on generated images from the low-resolution diffusion model. In various scenarios, we find that our model consistently outperforms DPM-Solver++ in terms of quality.

## 5 Conclusion and limitations

In this work, we present the Refined Exponential Solver (RES), derived from a meticulous analysis of numerical defects in diffusion model probability flow ODEs and fulfilling all order conditions. RES enjoys superior error bounds theoretically and enhanced sampling efficiency in practice. Originally designed to boost single-step updates, we have also extended the improvements to multistep schemes and stochastic samplers, effectively enhancing their performance.

Our work is also constrained by the following limitations. Our analysis reveals that the performance of different samplers is contingent on the trajectory of network evaluations along the exact solution, where a time-smooth trajectory facilitates the reduction of numerical error. However, existing works are still

uncertain about which time transformation or time scheduling leads to the most favorable trajectory. The logarithmic transformation we've used was selected based on our empirical observations. In practical terms, training-free methods still require more than 10 network evaluations, making them significantly slower than GANs or distillation-based methods. We leave it for future work to explore how distillation training can benefit from these improved training-free methods.

## References

- [1] Balaji, Y., Nah, S., Huang, X., Vahdat, A., Song, J., Kreis, K., Aittala, M., Aila, T., Laine, S., Catanzaro, B., et al. (2022). ediffi: Text-to-image diffusion models with an ensemble of expert denoisers. [arXiv preprint arXiv:2211.01324](#).
- [2] Bao, F., Li, C., Zhu, J., and Zhang, B. (2022). Analytic-DPM: An Analytic Estimate of the Optimal Reverse Variance in Diffusion Probabilistic Models.
- [3] Bautista, M. A., Guo, P., Abnar, S., Talbott, W., Toshev, A., Chen, Z., Dinh, L., Zhai, S., Goh, H., Ulbricht, D., et al. (2022). Gaudi: A neural architect for immersive 3d scene generation. [arXiv preprint arXiv:2207.13751](#).
- [4] Biloš, M., Rasul, K., Schneider, A., Nevmyvaka, Y., and Günnemann, S. (2022). Modeling temporal data as continuous functions with process diffusion. [arXiv preprint arXiv:2211.02590](#).
- [5] Chen, T., Liu, G.-H., and Theodorou, E. A. (2021a). Likelihood training of schrödinger bridge using Forward-Backward SDEs theory. [arXiv preprint arXiv:2110.11291](#).
- [6] Chen, Y., Georgiou, T. T., and Pavon, M. (2021b). Stochastic control liaisons: Richard sinkhorn meets gaspard monge on a schrodinger bridge. [SIAM Review](#), 63(2):249–313.
- [7] De Bortoli, V., Thornton, J., Heng, J., and Doucet, A. (2021). Diffusion schrödinger bridge with applications to Score-Based generative modeling. [arXiv preprint arXiv:2106.01357](#).
- [8] deep floyd (2023). If. <https://github.com/deep-floyd/IF>.
- [9] Dhariwal, P. and Nichol, A. (2021). Diffusion models beat GANs on image synthesis. [arXiv preprint arXiv:2105.05233](#).
- [10] Dockhorn, T., Vahdat, A., and Kreis, K. (2021). Score-Based generative modeling with Critically-Damped langevin diffusion. [arXiv preprint arXiv:2112.07068](#).
- [11] Efron, B. (2011). Tweedie’s formula and selection bias. [Journal of the American Statistical Association](#), 106(496):1602–1614.
- [12] Heusel, M., Ramsauer, H., Unterthiner, T., Nessler, B., and Hochreiter, S. (2017). GANs trained by a two Time-Scale update rule converge to a local nash equilibrium. [arXiv preprint arXiv:1706.08500](#).
- [13] Ho, J., Jain, A., and Abbeel, P. (2020). Denoising diffusion probabilistic models. [arXiv preprint arXiv:2006.11239](#).
- [14] Ho, J. and Salimans, T. (2022). Classifier-free diffusion guidance. [arXiv preprint arXiv:2207.12598](#).
- [15] Hochbruck, M. and Ostermann, A. (2005a). Explicit exponential runge–kutta methods for semilinear parabolic problems. [SIAM Journal on Numerical Analysis](#), 43(3):1069–1090.
- [16] Hochbruck, M. and Ostermann, A. (2005b). Exponential runge–kutta methods for parabolic problems. [Applied Numerical Mathematics](#), 53(2-4):323–339.
- [17] Hochbruck, M. and Ostermann, A. (2010). Exponential integrators. [Acta Numerica](#), 19:209–286.
- [18] Hoogeboom, E. and Salimans, T. (2022). Blurring diffusion models. [arXiv preprint arXiv:2209.05557](#).
- [19] Huang, C.-W., Lim, J. H., and Courville, A. C. (2021). A variational perspective on diffusion-based generative models and score matching. [Advances in Neural Information Processing Systems](#), 34:22863–22876.
- [20] Ilharco, G., Wortsman, M., Wightman, R., Gordon, C., Carlini, N., Taori, R., Dave, A., Shankar, V., Namkoong, H., Miller, J., Hajishirzi, H., Farhadi, A., and Schmidt, L. (2021). Openclip. If you use this software, please cite it as below.
- [21] Karras, T., Aittala, M., Aila, T., and Laine, S. (2022). Elucidating the design space of diffusion-based generative models. [arXiv preprint arXiv:2206.00364](#).
- [22] Kingma, D., Salimans, T., Poole, B., and Ho, J. (2021). Variational diffusion models. [Advances in neural information processing systems](#), 34:21696–21707.

- [23] Kong, Z. and Ping, W. (2021). On fast sampling of diffusion probabilistic models. [arXiv preprint arXiv:2106.00132](#).
- [24] Kong, Z., Ping, W., Huang, J., Zhao, K., and Catanzaro, B. (2020). Diffwave: A versatile diffusion model for audio synthesis. [arXiv preprint arXiv:2009.09761](#).
- [25] Li, S., Liu, L., Chai, Z., Li, R., and Tan, X. (2023). Era-solver: Error-robust adams solver for fast sampling of diffusion probabilistic models. [arXiv preprint arXiv:2301.12935](#).
- [26] Lin, C.-H., Gao, J., Tang, L., Takikawa, T., Zeng, X., Huang, X., Kreis, K., Fidler, S., Liu, M.-Y., and Lin, T.-Y. (2022). Magic3d: High-resolution text-to-3d content creation. [arXiv preprint arXiv:2211.10440](#).
- [27] Lin, T.-Y., Maire, M., Belongie, S., Hays, J., Perona, P., Ramanan, D., Dollár, P., and Zitnick, C. L. (2014). Microsoft coco: Common objects in context. In *Computer Vision–ECCV 2014: 13th European Conference, Zurich, Switzerland, September 6-12, 2014, Proceedings, Part V 13*, pages 740–755. Springer.
- [28] Lipman, Y., Chen, R. T., Ben-Hamu, H., Nickel, M., and Le, M. (2022). Flow matching for generative modeling. [arXiv preprint arXiv:2210.02747](#).
- [29] Liu, L., Ren, Y., Lin, Z., and Zhao, Z. (2022). Pseudo numerical methods for diffusion models on manifolds. [arXiv preprint arXiv:2202.09778](#).
- [30] Lu, C., Zhou, Y., Bao, F., Chen, J., Li, C., and Zhu, J. (2022a). Dpm-solver: A fast ode solver for diffusion probabilistic model sampling in around 10 steps. [arXiv preprint arXiv:2206.00927](#).
- [31] Lu, C., Zhou, Y., Bao, F., Chen, J., Li, C., and Zhu, J. (2022b). Dpm-solver++: Fast solver for guided sampling of diffusion probabilistic models. [arXiv preprint arXiv:2211.01095](#).
- [32] Luhman, E. and Luhman, T. (2021). Knowledge distillation in iterative generative models for improved sampling speed. [arXiv preprint arXiv:2101.02388](#).
- [33] Meng, C., Gao, R., Kingma, D. P., Ermon, S., Ho, J., and Salimans, T. (2022). On distillation of guided diffusion models. [arXiv preprint arXiv:2210.03142](#).
- [34] Poole, B., Jain, A., Barron, J. T., and Mildenhall, B. (2022). Dreamfusion: Text-to-3d using 2d diffusion. [arXiv preprint arXiv:2209.14988](#).
- [35] Press, W. H., Teukolsky, S. A., Vetterling, W. T., and Flannery, B. P. (2007). *Numerical recipes 3rd edition: The art of scientific computing*. Cambridge university press.
- [36] Qiao, Z., Nie, W., Vahdat, A., Miller III, T. F., and Anandkumar, A. (2022). Dynamic-backbone protein-ligand structure prediction with multiscale generative diffusion models. [arXiv preprint arXiv:2209.15171](#).
- [37] Rissanen, S., Heinonen, M., and Solin, A. (2022). Generative modelling with inverse heat dissipation. [arXiv preprint arXiv:2206.13397](#).
- [38] Rombach, R., Blattmann, A., Lorenz, D., Esser, P., and Ommer, B. (2022). High-resolution image synthesis with latent diffusion models. In *Proceedings of the IEEE/CVF Conference on Computer Vision and Pattern Recognition*, pages 10684–10695.
- [39] Russakovsky, O., Deng, J., Su, H., Krause, J., Satheesh, S., Ma, S., Huang, Z., Karpathy, A., Khosla, A., Bernstein, M., Berg, A. C., and Fei-Fei, L. (2015). ImageNet large scale visual recognition challenge. *International journal of computer vision*, 115(3):211–252.
- [40] Saharia, C., Chan, W., Saxena, S., Li, L., Whang, J., Denton, E., Ghasemipour, S. K. S., Ayan, B. K., Mahdavi, S. S., Lopes, R. G., et al. (2022). Photorealistic text-to-image diffusion models with deep language understanding. [arXiv preprint arXiv:2205.11487](#).
- [41] Salimans, T. and Ho, J. (2022). Progressive distillation for fast sampling of diffusion models. [arXiv preprint arXiv:2202.00512](#).
- [42] Seitzer, M. (2020). pytorch-fid: FID Score for PyTorch. <https://github.com/mseitzer/pytorch-fid>. Version 0.3.0.
- [43] Shue, J. R., Chan, E. R., Po, R., Ankner, Z., Wu, J., and Wetzstein, G. (2022). 3d neural field generation using triplane diffusion. [arXiv preprint arXiv:2211.16677](#).

- [44] Song, J., Meng, C., and Ermon, S. (2021a). Denoising diffusion implicit models. In International Conference on Learning Representations.
- [45] Song, Y., Dhariwal, P., Chen, M., and Sutskever, I. (2023). Consistency models. arXiv preprint arXiv:2303.01469.
- [46] Song, Y. and Ermon, S. (2020). Improved techniques for training Score-Based generative models. arXiv preprint arXiv:2006.09011.
- [47] Song, Y., Sohl-Dickstein, J., Kingma, D. P., Kumar, A., Ermon, S., and Poole, B. (2021b). Score-based generative modeling through stochastic differential equations. In International Conference on Learning Representations.
- [48] Tashiro, Y., Song, J., Song, Y., and Ermon, S. (2021). CSDI: Conditional score-based diffusion models for probabilistic time series imputation. Advances in Neural Information Processing Systems, 34:24804–24816.
- [49] Vahdat, A., Kreis, K., and Kautz, J. (2021). Score-based generative modeling in latent space. arXiv preprint arXiv:2106.05931.
- [50] Vargas, F., Thodoroff, P., Lamacraft, A., and Lawrence, N. (2021). Solving Schrödinger bridges via maximum likelihood. Entropy, 23(9):1134.
- [51] Vincent, P. (2011). A connection between score matching and denoising autoencoders. Neural computation, 23(7):1661–1674.
- [52] Wang, G., Jiao, Y., Xu, Q., Wang, Y., and Yang, C. (2021). Deep generative learning via schrödinger bridge. In International Conference on Machine Learning, pages 10794–10804. PMLR.
- [53] Wang, Z., Zheng, H., He, P., Chen, W., and Zhou, M. (2022). Diffusion-gan: Training gans with diffusion. arXiv preprint arXiv:2206.02262.
- [54] Watson, D., Ho, J., Norouzi, M., and Chan, W. (2021). Learning to efficiently sample from diffusion probabilistic models. arXiv preprint arXiv:2106.03802.
- [55] Wu, K. E., Yang, K. K., Berg, R. v. d., Zou, J. Y., Lu, A. X., and Amini, A. P. (2022). Protein structure generation via folding diffusion. arXiv preprint arXiv:2209.15611.
- [56] Xiao, Z., Kreis, K., and Vahdat, A. (2022). Tackling the generative learning trilemma with denoising diffusion GANs. In International Conference on Learning Representations (ICLR).
- [57] Xu, M., Yu, L., Song, Y., Shi, C., Ermon, S., and Tang, J. (2022). Geodiff: A geometric diffusion model for molecular conformation generation. arXiv preprint arXiv:2203.02923.
- [58] Zhang, Q. and Chen, Y. (2021). Diffusion normalizing flow. arXiv preprint arXiv:2110.07579.
- [59] Zhang, Q. and Chen, Y. (2022). Fast sampling of diffusion models with exponential integrator. arXiv preprint arXiv:2204.13902.
- [60] Zhang, Q., Tao, M., and Chen, Y. (2022). gddim: Generalized denoising diffusion implicit models. arXiv preprint arXiv:2206.05564.
- [61] Zhao, W., Bai, L., Rao, Y., Zhou, J., and Lu, J. (2023). Unipc: A unified predictor-corrector framework for fast sampling of diffusion models. arXiv preprint arXiv:2302.04867.

## A Related works and discussion

To unlock and democratize the extraordinary generative potential of diffusion models, considerable research efforts have been dedicated to enhancing their efficiency and speeding upsampling. In addition to the works discussed in Sec 1, other methods have been explored to enhance the speed of diffusion models.

The authors of [2] optimize the backward Markovian process to approximate the non-Markovian forward process, yielding an analytic expression of optimal variance in the denoising process. Another strategy involves making the forward diffusion nonlinear and trainable [58, 50, 7, 52, 5], in the spirit of the Schrödinger bridge [6]. However, this approach incurs a considerable training overhead. Researchers have also explored modifying the backward stochastic process by incorporating more function evaluations and optimizing time scheduling [23, 54]. Nevertheless, such acceleration strategies struggle to generate high-quality samples with a limited number of discretization steps. An alternate approach for improving diffusion models involves designing non-isotropic diffusion models, such as Blurring diffusion models [18, 37] and the critically-damped Langevin diffusion models [10]. There are other fast sampling methods by construction diffusion models in latent space [38, 49]. In addition, several works show GANs can be leveraged to accelerate diffusion models [56, 53].

More related are the diffusion model sampling algorithms inspired by semilinear ODEs solvers [59, 30]. Zhang and Chen [59] introduced Diffusion Exponential Integrator Sampler (DEIS), whose fastest variant is based on an approximate exact solution, achieved by replacing the nonlinear function with polynomial exploration. However, DEIS was originally designed for fitting polynomials in the original  $t$  space and is affected by noising scheduling  $\sigma(t)$ . On the other hand, Lu et al. [30] proposed DPM-Solver, which leverages a similar analysis of the exponential integrator to solve a semilinear ODE with time-varying coefficients. They further advanced DPM-Solver++ for the data prediction model and a sampling algorithm based on a multistep scheme, claiming improved sampling speed [31]. However, as we highlight in Sec 3.3, their numerical scheme does not meet all the necessary order conditions. The omission of these conditions could potentially worsen performance, especially with non-isotropic ODEs [17].

## B Proof

In this section, we provide detailed derivations and proofs for the key theoretical results presented in the paper. Given that we have two semi-linear ODEs Eq (7) and (8) sharing similar structures, we primarily concentrate on the data prediction model, with the understanding that the results can be easily extended to the ODE based on the noise prediction model. Recall that we denote the denoiser network as  $g$ , and its evaluation along the exact solution  $\mathbf{x}(\lambda)$  as  $f(\lambda) := g(\mathbf{x}(\lambda), \lambda)$ .

### B.1 Proof of Lemma 1

We first expand  $f$  into a Taylor series with the remainder in integral form,

$$f(\lambda_n + \tau) = \sum_{j=1}^q \frac{\tau^{j-1}}{(j-1)!} f^{(j-1)}(\lambda_n) + \int_0^\tau \frac{(\tau - \nu)^{q-1}}{(q-1)!} f^{(q)}(\lambda_n + \nu) d\nu \quad (18)$$

With Eq (18), we can rewrite exact ODE solution Eq (10) as

$$\begin{aligned} \mathbf{x}(\lambda_n + c_i h) &= e^{-c_i h} \mathbf{x}(\lambda_n) + \sum_{j=1}^{q_i} (c_i h)^j \phi_j(-c_i h) f^{(j-1)}(\lambda_n) \\ &\quad + \int_0^{c_i h} e^{-(c_i h - \tau)} \int_0^\tau \frac{(\tau - \nu)^{q_i-1}}{(q_i-1)!} f^{(q_i)}(\lambda_n + \nu) d\nu d\tau, \end{aligned} \quad (19)$$

where function  $\phi_j$  is defined as

$$\phi_j(-h) = \frac{1}{h^j} \int_0^h e^{\tau-h} \frac{\tau^{j-1}}{(j-1)!} d\tau, \quad j \geq 1. \quad (20)$$

With integration by part, we arrive at the recursion formulation for  $\phi$  function [17] as

$$\phi_{k+1}(z) = \begin{cases} \frac{\phi_k(z)-1/k!}{z} & k \geq 0, z \neq 0 \\ e^z & k = 0 \\ \frac{1}{k!}, & z = 0, k \leq 0 \end{cases}. \quad (21)$$

One the other hand, by integrating Eq (18) into the numerical scheme Eq (11), we can derive another expression for the exact solution. We begin with the exact solution at the intermediate time  $\lambda_n + c_i h$ . Plugging in Eq (18) into Eq (12a), we obtain

$$\begin{aligned} \mathbf{x}(\lambda_n + c_i h) &= e^{-c_i h} \mathbf{x}(\lambda_n) + h \sum_{k=1}^{i-1} a_{ik}(-h) \sum_{j=1}^{q_i} \frac{(c_k h)^{j-1}}{(j-1)!} f^{(j-1)}(\lambda_n) \\ &+ h \sum_{k=1}^{i-1} a_{ik}(-h) \int_0^{c_k h} \frac{(c_k h - \nu)^{q_i-1}}{(q_i-1)!} f^{(q_i)}(\lambda_n + \nu) d\nu d\tau + \delta_{n,i}. \end{aligned} \quad (22)$$

By comparing Eq (19) and Eq (22), we obtain the error term  $\Delta_{ni}$  as

$$\delta_{n,i} = \sum_{j=1}^{q_i} h^j \psi_{j,i}(-h) f^{(j-1)}(\lambda_n) + \delta_{n,i}^{(q_i)} \quad (23)$$

$$\psi_{j,i}(-h) = \phi_j(-c_i h) c_i^j - \sum_{k=1}^{i-1} a_{ik}(-h) \frac{c_k^{j-1}}{(j-1)!}, \quad (24)$$

where  $\delta_{n,i}^{(q_i)}$  denotes higher order terms that resulted from the truncation of the Taylor series.

Similarly, we can get the expression for  $\delta_{n+1}$  if we plug Eq (18) into Eq (12b) and comparing the result against Eq (19)

$$\delta_{n+1} = \sum_{j=1}^q h^j \psi_j(-h) f^{(j-1)}(\lambda_n) + \delta_{n+1}^{(q)} \quad (25)$$

$$\psi_j(-h) = \phi_j(-h) - \sum_{k=1}^s b_k(-h) \frac{c_k^{j-1}}{(j-1)!} \quad (26)$$

where  $\delta_{n+1}^{(q)}$  denotes higher order terms that resulted from the truncation of the Taylor series.

## C Proof of error bound

We first state several mild assumptions that are required for our theoretical bounds.

**Assumption 1.** For nonlinear function  $g : \mathbf{R}^d \times \mathbf{R} \rightarrow \mathbf{R}^d$  considered in this work, e.g.  $\epsilon_\theta, \mathbf{D}_\theta$ , we assume there exists a real number  $L(R)$  such that

$$\|g(\mathbf{x}_1, \lambda) - g(\mathbf{x}_2, \lambda)\| \leq L \|\mathbf{x}_1 - \mathbf{x}_2\|. \quad (27)$$

for all  $\lambda_{\min} \leq \lambda \leq \lambda_{\max}$  and  $\max(\|\mathbf{x}_1 - \mathbf{x}(\lambda)\|, \|\mathbf{x}_2 - \mathbf{x}(\lambda)\|) \leq R$  where  $\mathbf{x}(\lambda)$  is one ODE solution with nonlinear function  $g$ .

The region where  $\mathbf{x}_1, \mathbf{x}_2$  exists and is close to the exact solution is referred to as the strip along the exact ODE solution. For high-order methods, we introduce another assumption regarding the nonlinear function  $g$ :

**Assumption 2.** For ODE with nonlinear function  $g : \mathbf{R}^d \times \mathbf{R} \rightarrow \mathbf{R}^d$  considered in this work, e.g.  $\epsilon_\theta, \mathbf{D}_\theta$ ,  $g$  is differentiable in a strip along the ODE exact solution  $\mathbf{x}(\lambda)$ . All occurring derivatives are uniformly bounded.

By default, we assume that Thm 1 and 2 and Prop 1 satisfies above assumptions. First, we consider a scenario with a uniform step size, denoted as  $h$ . Subsequently, the obtained results are extended to accommodate non-uniform step sizes. This generalization involves loosening the error bounds'

reliance on the step size from the uniform case, directing it instead towards the maximum step size evident in the non-uniform scenario. Indeed, the error boundaries delineated in [Thm 1](#) and [2](#) manifest dependence on this longest step size.

First, we bound the truncated high-order term  $\delta_{n,i}^{(q_i)}$ . Based on [Eq \(19\)](#) and [\(22\)](#),  $\delta_{n,i}^{(q_i)}$  can be bounded by

$$\begin{aligned}
\|\delta_{n,i}^{(q_i)}\| &\leq \left\| \int_0^{c_i h} e^{-(c_i h - \tau)} \int_0^\tau \frac{(\tau - \nu)^{q_i - 1}}{(q_i - 1)!} f^{(q_i)}(\lambda_n + \nu) d\nu d\tau \right\| \\
&\quad + \left\| h \sum_{k=1}^{i-1} a_{ik}(-h) \int_0^{c_k h} \frac{(c_k h - \nu)^{q_i - 1}}{(q_i - 1)!} f^{(q_i)}(\lambda_n + \nu) d\nu \right\| \\
&\leq \sup_{\lambda \in [\lambda_n, \lambda_n + c_i h]} \|f^{(q_i)}\| \left( \left\| \int_0^{c_i h} e^{-(c_i h - \tau)} \int_0^\tau \frac{(\tau - \nu)^{q_i - 1}}{(q_i - 1)!} d\nu d\tau \right\| \right. \\
&\quad \left. + \left\| h \sum_{k=1}^{i-1} a_{ik}(-h) \int_0^{c_k h} \frac{(c_k h - \nu)^{q_i - 1}}{(q_i - 1)!} d\nu \right\| \right) \\
&\leq \sup_{\lambda \in [\lambda_n, \lambda_n + c_i h]} \|f^{(q_i)}\| C (c_i h)^{q_i + 1}, \tag{28}
\end{aligned}$$

where  $C$  is a sufficiently large constant. This is due to

$$\begin{aligned}
\left\| \int_0^{c_i h} e^{-(c_i h - \tau)} \int_0^\tau \frac{(\tau - \nu)^{q_i - 1}}{(q_i - 1)!} d\nu d\tau \right\| &\leq \left\| \int_0^{c_i h} d\tau \right\| \left\| \int_0^{c_i h} \frac{(c_i h - \nu)^{q_i - 1}}{(q_i - 1)!} d\nu \right\| = \frac{(c_i h)^{q_i + 1}}{(q_i)!} \\
\left\| h \sum_{k=1}^{i-1} a_{ik}(-h) \int_0^{c_k h} \frac{(c_k h - \nu)^{q_i - 1}}{(q_i - 1)!} d\nu \right\| &\leq \frac{\left\| \sum_{k=1}^{i-1} a_{ik}(-h) \right\| (c_i h)^{q_i + 1}}{c_i (q_i)!}.
\end{aligned}$$

We note above conclusion only holds when  $\psi_{j,i}(-h) = 0$  is satisfied. Otherwise, defects of  $h^j f^{(j-1)}(\lambda_n)$  will show up  $\|\delta_{n,i}^{(q_i)}\|$  once  $\psi_{j,i}(-h) \neq 0$ .

Similarly, we can bound the accumulation of  $\delta_i^{(q_i)}$  with

$$\left\| \sum_{j=0}^{n-1} e^{-jh} \delta_{n-j}^{(q_i)} \right\| \leq C h^{q_i} \sup_{\lambda \in [\lambda_1, \lambda_n]} \|f^{(q_i)}\| \tag{29}$$

once  $\phi_j = 0$  is satisfied. Indeed, the defect  $\delta_n^{(q)}$  can be formulated

$$\|\delta_n^{(q_i)}\| = \left\| \int_0^h e^{-(h-\tau)} \int_0^\tau \frac{(\tau - \nu)^{(q_i-1)}}{(q_i - 1)!} f^{(q_i)}(\lambda_{n-1} + \nu) d\nu d\tau \right\| \tag{30}$$

$$\leq \left\| \int_0^h e^{-(h-\tau)} d\tau \right\| \left\| \int_0^h \frac{(h - \nu)^{(q_i-1)}}{(q_i - 1)!} d\nu \right\| \sup_{\lambda \in [\lambda_{n-1}, \lambda_n]} \|f^{(q_i)}\| \tag{31}$$

$$= (1 - e^{-h}) \frac{h^{q_i}}{q_i!} \sup_{\lambda \in [\lambda_{n-1}, \lambda_n]} \|f^{(q_i)}\| \tag{32}$$

Therefore, we can bound

$$\begin{aligned}
\left\| \sum_{j=0}^{n-1} e^{-jh} \delta_{n-j}^{(q_i)} \right\| &\leq \sum_{j=0}^{n-1} \|e^{-jh} \delta_{n-j}^{(q_i)}\| \\
&\leq \left\| \sum_{j=0}^{n-1} e^{-jh} \right\| (1 - e^{-h}) \frac{h^{q_i}}{q_i!} \sup_{\lambda \in [\lambda_1, \lambda_n]} \|f^{(q_i)}\| \\
&\leq \frac{1}{1 - e^{-h}} (1 - e^{-h}) \frac{h^{q_i}}{q_i!} \sup_{\lambda \in [\lambda_1, \lambda_n]} \|f^{(q_i)}\| \\
&= \frac{h^{q_i}}{q_i!} \sup_{\lambda \in [\lambda_1, \lambda_n]} \|f^{(q_i)}\| \leq C h^{q_i} \sup_{\lambda \in [\lambda_1, \lambda_n]} \|f^{(q_i)}\|,
\end{aligned}$$

with a sufficiently large  $C$ .

Second, we introduce Discrete Gronwall Inequality in [Lemma 2](#), which we will use later.

**Lemma 2** (Discrete Gronwall Inequality). *Let  $\langle \alpha_n \rangle$  and  $\langle \beta_n \rangle$  be nonnegative sequences and  $c$  a nonnegative constant. If*

$$\alpha_n \leq c + \sum_{0 \leq k < n} \beta_k \alpha_k,$$

then

$$\alpha_n \leq c \prod_{0 \leq j < n} (1 + \beta_j) \leq c \exp\left(\sum_{0 \leq j < n} \beta_j\right) \quad \text{for } n \geq 0. \quad (33)$$

### C.1 Order 1 error bound for [Thm 1](#)

With [Lemma 1](#), we can formulate the error recursion for the  $s = 1$  case

$$\Delta_{n+1} = e^{-h} \Delta_n + h\phi_1(-h)(g(\mathbf{x}_n, t_n) - f(t_n)) - \delta_{n+1} \quad (34)$$

with defects  $\delta_{n+1} = \delta_{n+1}^{(1)}$ , the recursion gives

$$\Delta_n = h \sum_{j=0}^{n-1} e^{-(n-j-1)h} \phi_1(-h)(g(\mathbf{x}_j, t_j) - f(t_j)) - \sum_{j=0}^{n-1} e^{-jh} \delta_{n-j}. \quad (35)$$

Thanks to [Assumption 1](#) and [Eq \(29\)](#), we can bound above  $\Delta_n$  by

$$\|\Delta_n\| \leq \sum_{j=1}^{n-1} h\phi_1(-h)e^{-(n-j-1)h} L \|\Delta_j\| + Ch \sup_{\lambda \in [\lambda_n, \lambda_n + c_1 h]} \|f^{(1)}\| \quad (36)$$

With Discrete Gronwall Inequality [Lemma 2](#) and  $\Delta_0 = 0$ , we can show that

$$\|\Delta_n\| = \|\mathbf{x}_n - \mathbf{x}(\lambda_n)\| \leq Ch \sup_{\lambda_{\min} \leq \lambda \leq \lambda_{\max}} \|f'(\lambda)\| \exp\left(\prod_{j=1}^{n-1} hL\phi_1(-h)e^{-(n-j-1)h}\right) \quad (37)$$

$$\leq Ch \sup_{\lambda_{\min} \leq \lambda \leq \lambda_{\max}} \|f'(\lambda)\| \exp(L^n) \quad (38)$$

$$\leq C'h \sup_{\lambda_{\min} \leq \lambda \leq \lambda_{\max}} \|f'(\lambda)\| \quad (39)$$

with a large enough  $C'$ . This finishes the proof for [Thm 1](#) if we upper bound [Eq \(39\)](#) by the largest step size in the non-uniform stepsize case. Thanks to order condition  $\psi_1 = 0$  and  $c_1 = 0$ , the Butcher tableau follows

$$\begin{array}{c|c} 0 & \\ \hline & \phi_1(-h). \end{array} \quad (40)$$

### C.2 High order error bounds

We first start with the second order method. Since it is a second-stage algorithm, we have only one intermediate point  $\mathbf{x}_{n,1}$ . Based on [Eq \(13\)](#) and [\(28\)](#) and [Assumption 1](#), we can bound

$$\|\Delta_{n,2}\| \leq C_1 \|\Delta_n\| + \|\delta_{n,2}^{(1)}\| \quad (41)$$

$$\leq C_1 \|\Delta_n\| + C_2 h^2 \sup_{\lambda \in [\lambda_n, \lambda_n + c_2 h]} \|f^{(1)}\|, \quad (42)$$

where  $C_1, C_2$  are two constants. And we know  $\Delta_{n,1} = \Delta_n$  for our explicit method due to  $c_1 = 0$ .

Similar to [Eq \(36\)](#), we can bound

$$\begin{aligned} \|\Delta_n\| &\leq h \sum_{j=0}^{n-1} e^{-(n-j-1)h} \phi_1(-h) C_3 \max(\|\Delta_j\|, \|\Delta_{j,1}\|) + \sum_{j=0}^{n-1} e^{-jh} \delta_{n-j} \\ &\leq h \sum_{j=0}^{n-1} e^{-(n-j-1)h} \phi_1(-h) C_4 \|\Delta_j\| + h \sum_{j=0}^{n-1} e^{-(n-j-1)h} \phi_1(-h) C_2 h^2 \sup_{\lambda \in [\lambda_{\min}, \lambda_{\max}]} \|f^{(1)}\| \\ &\quad + C_5 h^2 \sup_{\lambda \in [\lambda_{\min}, \lambda_{\max}]} \|f^{(2)}\|, \end{aligned}$$

where  $C_4 = \max(1, C_1)$ , and the last inequality is due to [Eq \(29\)](#). We note that  $h \sum_{j=0}^{n-1} e^{(-n-j-1)h} \phi_1(-h) \leq 1$ . We can further simplify the upper bound of  $\Delta_n$  by

$$\begin{aligned} \|\Delta_n\| &\leq h \sum_{j=0}^{n-1} e^{(-n-j-1)h} \phi_1(-h) C_4 \|\Delta_j\| \\ &\quad + \max(C_2, C_5) h^2 \left( \sup_{\lambda \in [\lambda_{min}, \lambda_{max}]} \|f^{(2)}\| + \sup_{\lambda \in [\lambda_{min}, \lambda_{max}]} \|f^{(1)}\| \right). \end{aligned}$$

Due to [Lemma 2](#), we can upper bound it by

$$\|\Delta_n\| \leq \max(C_2, C_5) h^2 \left( \sup_{\lambda \in [\lambda_{min}, \lambda_{max}]} \|f^{(2)}\| + \sup_{\lambda \in [\lambda_{min}, \lambda_{max}]} \|f^{(1)}\| \right) \quad (43)$$

$$\begin{aligned} &\exp \left( \prod_{j=1}^{n-1} C_4 h \phi_1(-h) e^{-(n-j-1)h} \right) \\ &\leq C' h^2 \left( \sup_{\lambda \in [\lambda_{min}, \lambda_{max}]} \|f^{(2)}\| + \sup_{\lambda \in [\lambda_{min}, \lambda_{max}]} \|f^{(1)}\| \right) \end{aligned} \quad (44)$$

for a large enough  $C'$ . This finishes the proof of [Thm 2](#) if we upper bound [Eq \(39\)](#) by the largest step size in the non-uniform stepsize case.

Thanks to condition  $\psi_1(-h) = \psi_2(-h) = \psi_{1,2}(-h) = 0$ , the Butcher tableau has to satisfy

$$\begin{aligned} b_1 + b_2 &= \phi_1(-h) \\ b_2 c_2 &= \phi_2(-h) \\ a_{21} &= c_2 \phi_1(-c_2 h). \end{aligned}$$

Therefore, the only solution for Butcher tableau is

$$\begin{array}{c|c} 0 & \\ c_2 & c_2 \phi_1(-c_2 h) \\ \hline 0 & \phi_1(-h) - \frac{1}{c_2} \phi_2(-h) \quad \frac{1}{c_2} \phi_2(-h) \end{array}. \quad (45)$$

For third-order methods, numerical methods with three-stage methods have to satisfy [\[15, Sec 5.2\]](#)

$$\begin{aligned} \psi_1(-h) &= 0 \\ \psi_2(-h) &= 0 \\ \psi_{1,2}(-h) &= 0 \\ \psi_{1,3}(-h) &= 0 \\ \psi_3(-h) &= 0 \\ b_2 \psi_{2,2}(-h) + b_3 \psi_{2,3}(-h) &= 0 \end{aligned}$$

One two-parameter solution family for Butcher tableau satisfies other conditions and achieves third-order error bounds follows

$$\begin{array}{c|c} 0 & \\ c_2 & c_2 \phi_{1,2} \\ c_3 & c_3 \phi_{1,3} - a_{32} \quad \frac{c_3^2}{c_2^2} \phi_{2,3} \\ \hline & \phi_1 - b_2 - b_3 \quad 0 \quad \frac{1}{c_3} \phi_2 \end{array}, \quad (46)$$

where  $\gamma$  can be obtained by solving  $2(\gamma c_2 + c_3) = 3(\gamma c_2^2 + c_3^3)$  once  $c_2, c_3$  are given.

## D Algorithms

For deterministic single-step and stochastic samplers, we have listed the unified algorithm in [Alg 2](#). We have also listed the algorithm for single-step second order update in [Alg 1](#). Furthermore, we list general high order algorithm in [Alg 3](#).

---

**Algorithm 3** RES General  $s$ -stage Single-step Update with  $\{c_s\}$ 

---

```
1: procedure SINGLEUPDATESTEP( $\mathbf{x}_n, \sigma_n, \sigma_{n+1}$ )
2:    $\lambda_{n+1}, \lambda_n \leftarrow -\log(\sigma_{n+1}), -\log(\sigma_n)$ 
3:    $h \leftarrow \lambda_{n+1} - \lambda_n$  ▷ Step length
4:    $\{a_{ij}\}, \{b_j\} \leftarrow$  Butcher tableau with  $\{c_i\}$  ▷ Single-step update coefficients
5:    $(\mathbf{x}_{n,1}, \lambda_{n,1}) \leftarrow (\mathbf{x}_n, \lambda_n)$  ▷  $c_1 = 0$  for explicit methods
6:   for  $i$  in  $2, \dots, s$  do
7:      $(\mathbf{x}_{n,i}, \lambda_{n,i}) \leftarrow (e^{-c_i h} \mathbf{x}_n + h \sum_{j=1}^i a_{i,j} \mathbf{D}_\theta(\mathbf{x}_{n,j}, \lambda_n + c_j h), \lambda_n + c_i h)$ 
8:    $\mathbf{x}_{n+1} \leftarrow e^{-h} \mathbf{x}_n + h(\sum_{i=1}^s b_i \mathbf{D}_\theta(\mathbf{x}_{n,i}, \lambda_n + c_i h))$ 
9:   return  $\mathbf{x}_{n+1}$ 
```

---

---

**Algorithm 4** RES Second order Multistep Update Scheme

---

```
1: procedure MULTISTEPUPDATE( $\mathbf{x}_n, \sigma_n, \sigma_{n+1}, \mathbf{D}_\theta(\mathbf{x}_{n-1}, \lambda_{n-1})$ )
2:    $\lambda_{n+1}, \lambda_n, \lambda_{n-1} \leftarrow -\log(\sigma_{n+1}), -\log(\sigma_n), -\log(\sigma_{n-1})$ 
3:    $h \leftarrow \lambda_{n+1} - \lambda_n$  ▷ Step length
4:    $c_2 \leftarrow \frac{\lambda_{n-1} - \lambda_n}{h}$ 
5:    $b_1, b_2 \leftarrow \phi_1(-h) - \phi_2(-h)/c_2, \phi_2(-h)/c_2$  ▷ Coefficients
6:    $\mathbf{x}_{n+1} \leftarrow e^{-h} \mathbf{x}_n + h(b_1 \mathbf{D}_\theta(\mathbf{x}_n, \lambda_n) + b_2 \mathbf{D}_\theta(\mathbf{x}_{n-1}, \lambda_{n-1}))$ 
7:   return  $\mathbf{x}_{n+1}$ 
```

---

### D.1 Multistep algorithm

The insights and analysis gained from a multi-stage single-step numerical scheme can be leveraged to develop multistep numerical methods. The crux of a multistep update step lies in its utilization of not only the function evaluation at the current state but also previous function evaluations.

To underscore the parallels between single-step and multistep methods, consider a single update step from timestamp  $\lambda_n$  to  $\lambda_{n+1} := \lambda_n + h$  with function evaluations  $\{g(\mathbf{x}_{n,i}, \lambda_n + c_i h)\}_{i=1}^r$ , where  $c_1 = 0, c_i < 0$  for  $1 < i \leq r$  and  $\mathbf{x}_{n,i}$  are numerical results on timestamp  $\lambda_n + c_i h$ . The general multistep scheme can be expressed as follows:

$$\mathbf{x}_{n+1} = e^{-h} \mathbf{x}_n + h \left[ \sum_{i=1}^r b_i g(\mathbf{x}_{n,i}, \lambda_n + c_i h) \right] \quad (47)$$

The present multistep method configuration bears many resemblances to the single-step method outlined in [Sec 3.2](#). The distinction resides in the selection of  $\{c_i\}_{i=2}^r$ , which are chosen such that  $\lambda_n + c_i h = \lambda_{n+1-i}$ . Consequently, with  $\mathbf{x}_{n,i}$  coinciding with  $\mathbf{x}_{n+1-i}$ , we can bypass the function evaluation cost, as  $g(\mathbf{x}_{n,i}, \lambda_n + c_i h)$  is readily available due to the existing value of  $g(\mathbf{x}_{n+1-i}, \lambda_{n+1-i})$ .

From this viewpoint, the construction of auxiliary  $\hat{\mathbf{x}}$  and intermediate numerical defects  $\delta_n$  in [Sec 3.2](#) remain applicable for multistep cases. Most notably, the error recursion in [Eq \(13a\)](#) and the expansion of  $\delta_{n+1}$  in [Lemma 1](#) persist in the multistep scenario. To minimize numerical defects, we also aim to reduce  $\delta_n$ . Therefore, the choice of  $b_i$  from the Butcher tableaux developed for the single-step scheme can be employed for multistep methods with particular  $c_i$  values. The second-order multistep algorithm is detailed in [Alg 4](#).

## E Experiment details

In this section, we provide necessary experiments details and extra experiments.

### E.1 Reproduction of [Fig 1](#)

**Fig 1a** We use the pre-trained ImageNet  $64 \times 64$  class-conditioned diffusion model [\[21\]](#) to conduct the experiment. Due to the lack of ground truth solution trajectories, we use high-accuracy ODE solvers to approximate the solutions. Concretely, we employ RK4 with 500 steps (2000 NFE) to generate trajectories, with negligible alterations with more steps. To generate those trajectories, we randomly select initial random noise and labels. Curves in [Fig 1a](#) are averaged over 512 trajectories.

NFE	DDIM (S)	Heun (S)	DPM-Solver++ (S)	Our (S)	DPM-Solver++ (M)	Our (M)
6	2515	$1.446 \times 10^4$ *	2681*	1774*	1507	2602
8	2063	3943*	2060*	1072*	1062	1895
10	1747	2501*	1544*	729.1*	740.2	1195
15	1280	992.7	845.7	382.6	369.9	463.3
20	1020	623.9*	617.8*	283.6*	227.6	258.7
25	852.7	360.4	420.7	187.6	153.2	167.8
30	731.4	270.4*	339.4*	151.1*	114	117.1
35	640.1	190.2	256.5	113.8	87.17	85.13
50	468.4	106.3*	146*	64.43*	46.06	40.59
75	328.1	43.23	68.56	31.35	22.82	18.28
100	254.6	24.56*	41.63*	19.08*	14.58	10.65

**Table 4:** Numerical defects  $|\mathbf{x}(0) - \mathbf{x}_N|$  with different NFEs and recommended time scheduling for Fig 2 (Left). \* indicates the number is produced by one less NFE.

**Extra experiments** Besides the “acceleration” outlined in Fig 1a, we examine the evolution of  $f(\lambda) := g(\mathbf{x}(\lambda), \lambda)$  along the solution trajectory for various nonlinear functions  $g$ . We note that smoother  $f$  typically results in smaller numerical defects, as indicated in Lemma 1 and Thm 1 and 2. As depicted in Fig 5, the benefit of applying a logarithmic transformation to the noise level  $\sigma$  is evident.

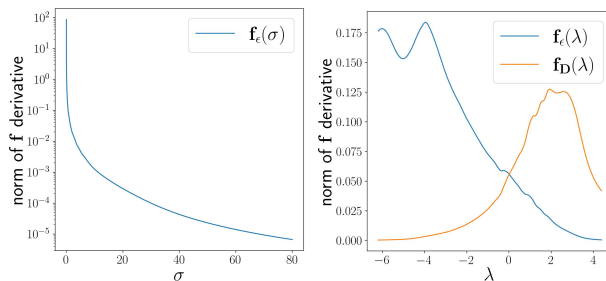


**Figure 5:** (Left) The evolution of nonlinear function evaluation for Eq (6) characterized by  $f_\epsilon(\sigma) := \epsilon_\theta(\mathbf{x}(\sigma), \sigma)$ . (Right) The evolution of nonlinear function evaluation for Eq (8), defined by  $f_\epsilon(\lambda) := \epsilon_\theta(\mathbf{x}(\lambda), \lambda)$  and  $f_D(\lambda) := D_\theta(\mathbf{x}(\lambda), \lambda)$ . Implementing a logarithmic transformation on the noise level  $\sigma$  results in smoother trajectories of nonlinear function evaluations along ODE solutions.

## E.2 Reproduction of Fig 2

We utilize the pre-trained ImageNet  $64 \times 64$  class-conditioned diffusion model [21] for our experiment. For the numerical defect experiments, we approximate the ground truth solution  $\mathbf{x}(0)$  using 500 steps RK4 (2000 NFE). We generate 50,000 images with randomized labels to calculate numerical defects and FIDs. The EDM, as suggested by Karras et al. [21], follows a time schedule as given in Eq (48),

$$t_i = (\sigma_{\max}^{\frac{1}{\rho}} + \frac{i}{N-1}(\sigma_{\min}^{\frac{1}{\rho}} - \sigma_{\max}^{\frac{1}{\rho}}))^{\rho}, \quad (48)$$

where  $\rho$  is a hyperparameter that controls the timestamp spacing. Our findings reveal that the  $\epsilon_\theta$ -based RES outperforms the  $D_\theta$ -based RES. By default, we adhere to the recommended  $\rho = 7$  for our experiments. To test the robustness through the suboptimal time rescheduling experiment, we use  $\rho = 1$ , where the timestamps are uniformly distributed in  $\sigma$ . For all experiments, we test the sampling algorithm with NFE set to 6, 8, 10, 15, 20, 25, 30, 35, 50, 75, 100. Similar to EDM, an additional denoising step is included in the final stage. We note that for second-order single-step methods, the total NFE may not align perfectly with the NFE. In such instances, we always take one less step, for example, second-order methods only use 5 NFEs when we expect them to utilize 6 NFEs. We use the official code from Karras et al. [21] to calculate FID score. We include quantitative results in Tab 4 to 6.

NFE	DDIM (S)	Heun (S)	DPM-Solver++ (S)	Our (S)	DPM-Solver++ (M)	Our (M)
6	41.09	248.3*	68.97*	56.46*	14.87	14.32
8	25.12	86.88*	28.33*	19.4*	8.024	7.44
10	17.26	35.32*	16.77*	8.665*	5.456	5.115
15	9.284	5.544	6.402	3.944	3.525	3.23
20	6.446	3.682*	4.593*	3.298*	2.975	2.542
25	5.101	2.899	3.493	2.885	2.726	2.412
30	4.348	2.705*	3.151*	2.742*	2.602	2.377
35	3.712	2.571	2.86	2.607	2.523	2.346
50	3.18	2.431*	2.575*	2.471*	2.425	2.336
75	2.968	2.406	2.514	2.436	2.401	2.335
100	2.755	2.381	2.453	2.401	2.377	2.333

**Table 5:** FID with different NFEs and recommended time scheduling for Fig 2 (Mid). \* indicates the number is produced by one less NFE.

NFE	DDIM (S)	Heun (S)	DPM-Solver++ (S)	Our (S)	DPM-Solver++ (M)	Our (M)
6	2339	$4.116 \times 10^4$ *	2850*	1957*	5034	4615
8	1948	$1.249 \times 10^4$ *	2004*	1177*	5281	5430
10	1664	5901*	1578*	827.9*	5296	5800
15	1241	1362	907.2	435.6	4975	5469
20	996.9	780.2*	681*	314.8*	4445	4779
25	834.9	428	483.1	222.6	3923	4116
30	718.5	312.7*	392.9*	184.8*	3513	3675
35	632.6	218.3	300.5	139.6	3191	3409
50	467.5	126.1*	185.6*	90.87*	2597	2607
75	329.4	79.22	101.2	55.01	2019	1876
100	256.8	63.15*	70.82*	43.44*	1658	1537

**Table 6:** Numerical defects  $|\mathbf{x}(0) - \mathbf{x}_N|$  with different NFEs and suboptimal time scheduling for Fig 2 (Right). \* indicates the number is produced by one less NFE.

### E.3 Reproduction of Fig 3

We utilize pre-trained diffusion models equipped with a noise data classifier from Dhariwal and Nichol [9]. These diffusion models are trained on discrete time analogous to DDPM. By employing an additional noise data classifier  $p(\mathbf{c}|\mathbf{x})$ , we can derive a new diffusion model by incorporating the gradient of the classifier into the diffusion model, resulting in the following denoiser:

$$\hat{D}(\mathbf{x}, \sigma|\mathbf{c}) = \mathbf{x} + \sigma^2 \nabla_{\mathbf{x}} \log p(\mathbf{x}|\mathbf{c}; \sigma) \quad (49)$$

$$= \mathbf{x} + \sigma^2 \nabla_{\mathbf{x}} \log p(\mathbf{x}; \sigma) + \sigma^2 \nabla_{\mathbf{x}} \log p(\mathbf{c}|\mathbf{x}; \sigma), \quad (50)$$

where  $p(\mathbf{c}|\mathbf{x}; \sigma)$  denotes a classifier for the label  $\mathbf{c}$  on noise data. In practice, researchers have observed that increasing the weight on the classifier can enhance performance, as expressed by:

$$\hat{D}(\mathbf{x}, \sigma|\mathbf{c}) \approx \hat{D}_{\theta}(\mathbf{x}, \sigma|\mathbf{c}) + \omega \sigma^2 \nabla_{\mathbf{x}} \log p(\mathbf{y}|\mathbf{x}; \sigma), \quad (51)$$

where  $\omega$  can be adjusted to values greater than 1. In our experiment, we utilize the pre-trained classifier detailed in Dhariwal and Nichol [9]. We approximate the ground truth  $\mathbf{x}(0)$  using 500 steps of the RK4 method. In addition, we apply dynamic thresholding [40] to all methods evaluated in this experiment to ensure a fair comparison. We conduct the sampling tests with NFE values of 6, 7, 8, 9, 10, 12, 15, 18, 20, 30, 50. It should be noted that for guided diffusion models, our approach based on  $D_{\theta}$  proves superior. We use the official code from Dhariwal and Nichol [9] to calculate FID score.

### E.4 Reproduction of Fig 4a

This experiment is designed to demonstrate how an enhanced single-step sampler can augment stochastic samplers' performance. We utilize the pre-trained ImageNet  $64 \times 64$  class-conditioned diffusion model [21] for this purpose. The time schedule adheres to the recommended setting with  $\rho = 7$ . With a fixed level of stochasticity, parameterized by  $\eta$ , we contrast the second order Heun method with our method at NFE values of 6, 8, 10, 15, 20, 25, 30, 35, 50, 75, 100, 150, 200, 350, 500.

We also examine the influence of  $\eta$  on the FID with a fixed NFE of 75, iterating  $\eta = 0, 0.01, 0.025, 0.05, 0.15, 0.20, 0.30, 0.35, 0.40, 0.45, 0.50$ . We observe that adding random noise can enhance perceptual quality in terms of FID when compared to deterministic sampling, although an excess of stochasticity can impair sampling quality. We use the official code from Karras et al. [21] to calculate FID score.

### E.5 Reproduction of Fig 4b

This experiment is designed to corroborate the effectiveness of our enhanced order analysis and RES in large-scale text-to-image diffusion models [8], primarily against the benchmark set by DPM-Solver++ [31]. The initial experiments examine FID-CLIP scores under varying classifier-free guidance weights [14]. With classifier-free guidance, we can build a new diffusion model based on a conditional diffusion model and an unconditional model. Specifically, for either the data prediction model or the noise prediction model, denoted by their network as  $g$ , the newly proposed diffusion model adheres to the following protocol:

$$\hat{g}(\mathbf{x}, \sigma, \mathbf{c}) := g(\mathbf{x}, \sigma, \emptyset) + \omega(g(\mathbf{x}, \sigma, \mathbf{c}) - g(\mathbf{x}, \sigma, \emptyset)), \quad (52)$$

where  $\omega$  serves as the guidance weight,  $\emptyset$  represents the unconditional signal, and  $\mathbf{c}$  stands for the conditional signal<sup>1</sup>. We vary the guidance between 1, 1.5, 3, 5, 10. We employ ViT-g-14 [20] for the calculation of the CLIP score and `pytorch-fid` for FID. This experiment is carried out on the MS-COCO validation dataset. Owing to computational resource constraints, the experiment is performed at a resolution of  $64 \times 64$  with a fixed 25 NFE. It should be noted that for this experiment, we merely substitute the degenerated Butcher tableau of DPM-Solver++ with our Butcher tableau, keeping all other configurations consistent. The experiment is based on [IF-I-XL](#).

In a further experiment, we compare RES and DPM-Solver++ using the upsampling diffusion model [IF-II-L](#), which upsamples a low-resolution image of  $64 \times 64$  pixels to a high-resolution image of  $256 \times 256$  pixels. For this test, we feed generated  $64 \times 64$  images, using the single-step RES with 49 NFE, along with corresponding captions into the upsampling model. We then vary the NFE to assess the quality of the generated images. Intriguingly, our findings reveal that the single-step RES outperforms multi-step methods in terms of the quality of samples produced.

In our experiments involving DeepFloyd IF models, we adopt the time schedule outlined in [Eq \(48\)](#) with  $\rho = 7$ . Owing to constraints on our computational resources, we are unable to sweep through hyperparameters to locate a more optimized time schedule. However, we posit that with the same NFE, the quality of the sampling could be further enhanced by fine-tuning the time schedule.

### E.6 Licenses

#### Dataset

- ImageNet [39]      The license status is unclear
- MS-COCO [27]      Creative Commons Attribution 4.0 License.

#### Pre-trained models and code

- EDM ImageNet [21]      Creative Commons Attribution-NonCommercial-ShareAlike 4.0 International License
- DeepFloyd IF [8]      DeepFloyd IF License Agreement
- OpenAI Guided ImageNet [9]      MIT License
- Pytorch FID [42]      Apache License 2.0
- OpenCLIP [20]      MIT License

## F Image samples

In this section, we include samples from our experiments for quantitative comparison.

<sup>1</sup>We slightly modify the classifier-free equation to align it with the implementation [8] available at [https://github.com/deep-floyd/IF/blob/2ad4dff7cde3cce91f237270a3cc81cae4578015/deepfloyd\\_if/modules/base.py#L114](https://github.com/deep-floyd/IF/blob/2ad4dff7cde3cce91f237270a3cc81cae4578015/deepfloyd_if/modules/base.py#L114)

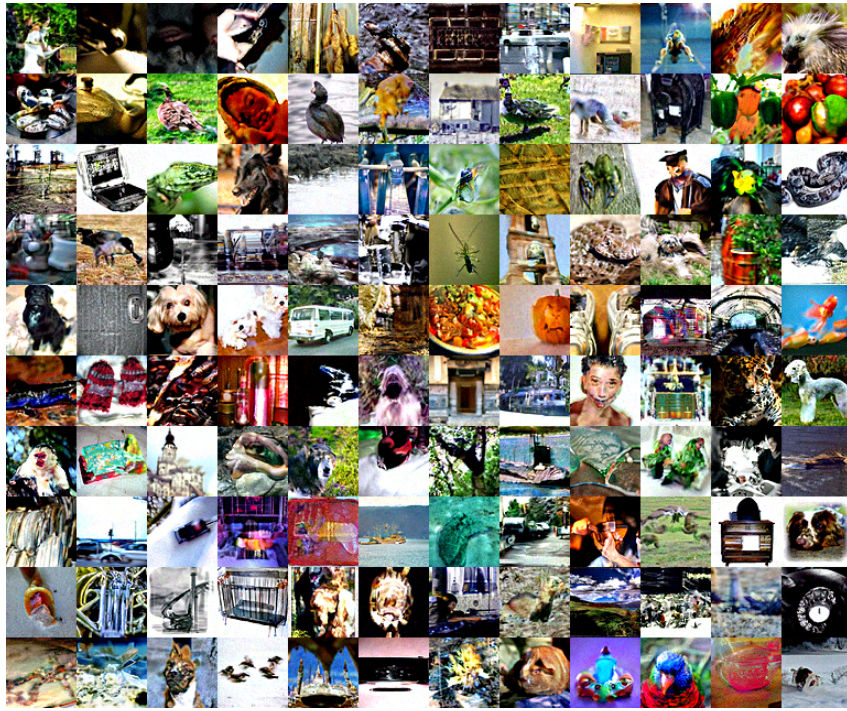


**Figure 6:** Uncurated samples of  $64 \times 64$  ImageNet model [21] with single-step Heun 9 NFE. (FID=35.31)

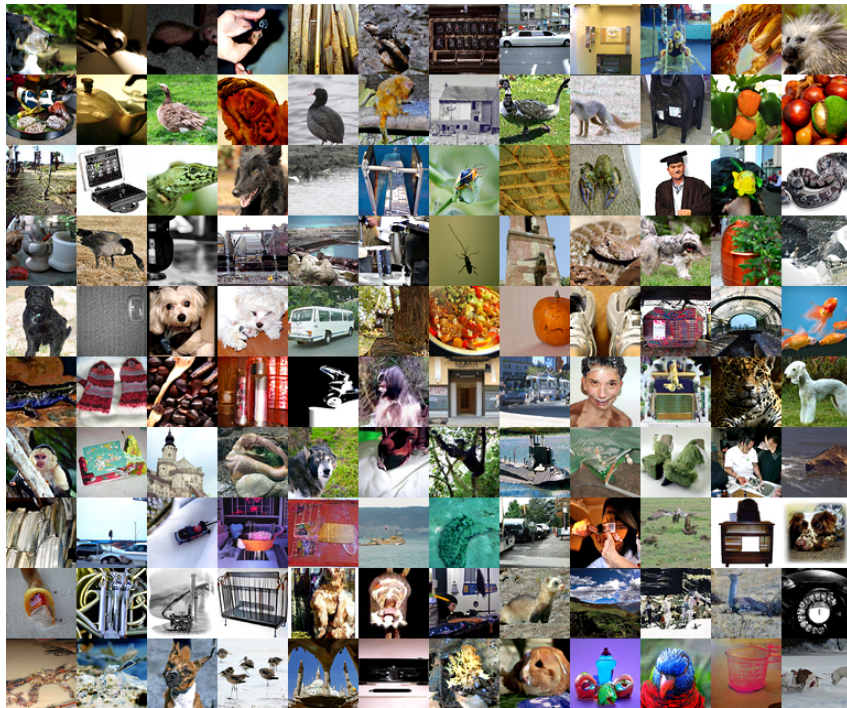


**Figure 7:** Uncurated samples of  $64 \times 64$  ImageNet model [21] with single-step Heun 15 NFE. (FID=5.54)

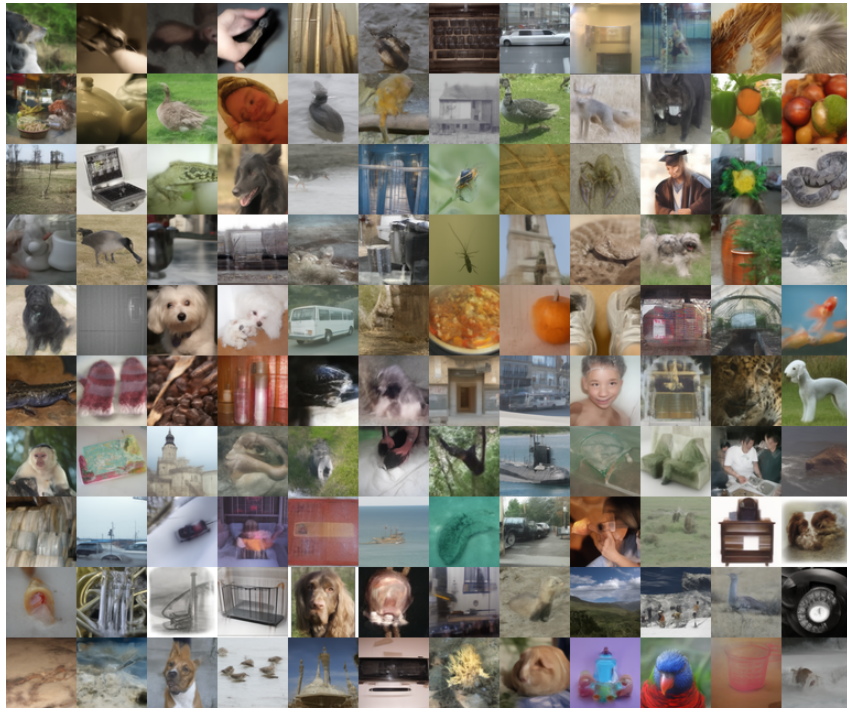


**Figure 8:** Uncurated samples of  $64 \times 64$  ImageNet model [21] with single-step DPM-Solver++ 9 NFE. (FID=16.77)

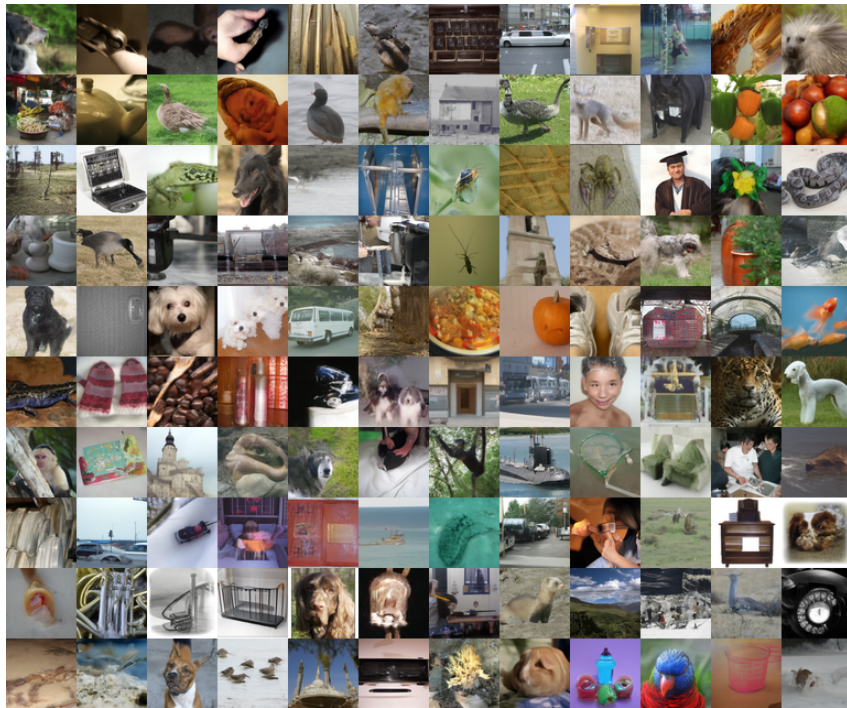


**Figure 9:** Uncurated samples of  $64 \times 64$  ImageNet model [21] with single-step DPM-Solver++ 15 NFE. (FID=6.40)

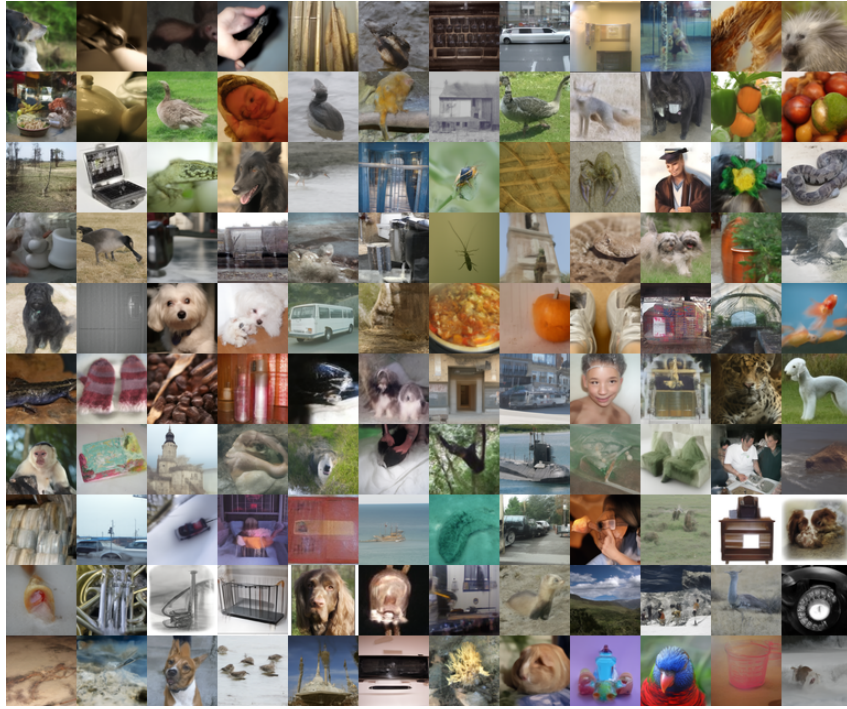


**Figure 10:** Uncurated samples of  $64 \times 64$  ImageNet model [21] with single-step RES data prediction model 9 NFE. (FID=8.66)

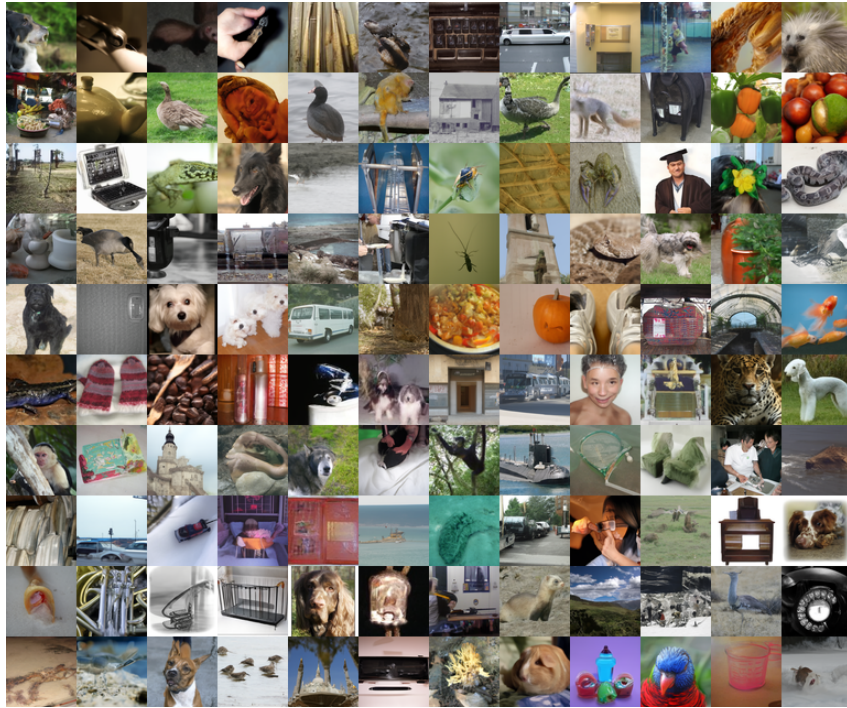


**Figure 11:** Uncurated samples of  $64 \times 64$  ImageNet model [21] with single-step RES data prediction model 15 NFE. (FID=3.92)

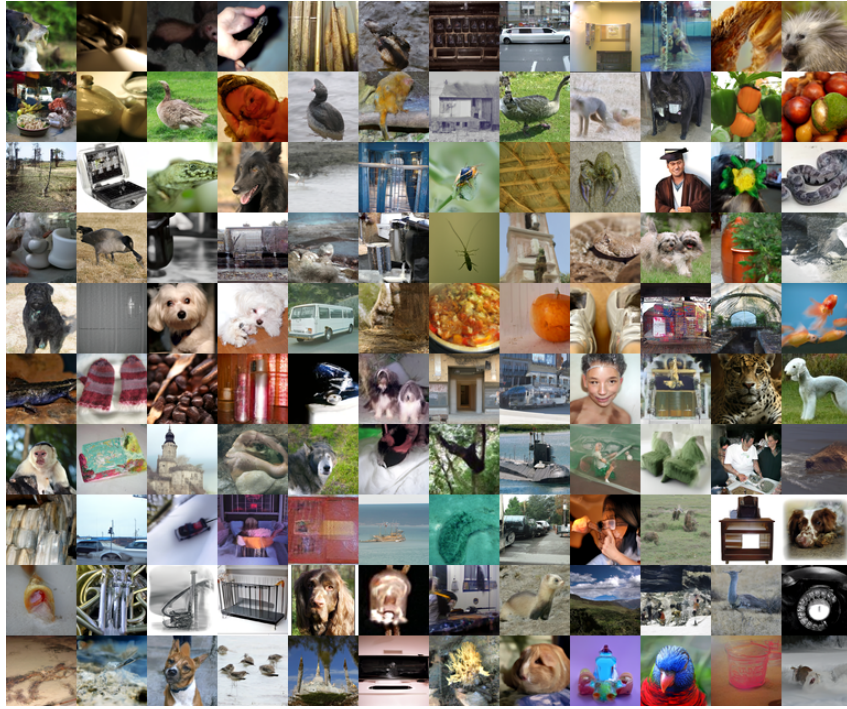


**Figure 12:** Uncurated samples of  $64 \times 64$  ImageNet model [21] with single-step RES noise prediction model 9 NFE. (FID=5.08)

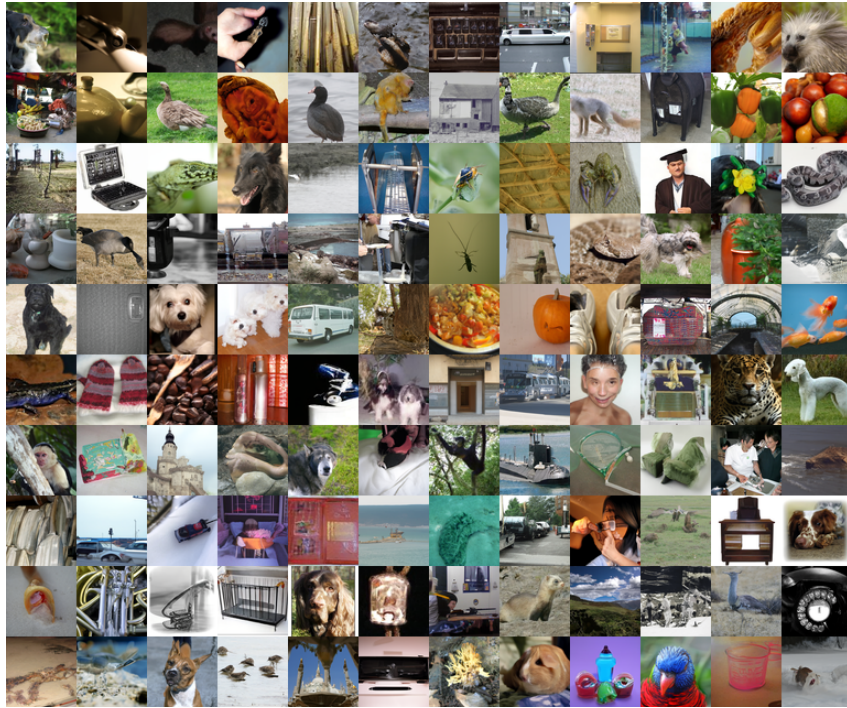


**Figure 13:** Uncurated samples of  $64 \times 64$  ImageNet model [21] with single-step RES noise prediction model 15 NFE. (FID=3.88)



Uncurated samples of  $256 \times 256$  DeepFloyd IF model with single-step DPM++ 19 NFE (MS-COCO validation FID=24.57)



Uncurated samples of  $256 \times 256$  DeepFloyd IF model with single-step RES19 NFE (MS-COCO validation FID=24.21)



**Figure 14:** Single-step DPM-Solver++ vs Single-step RES on cascaded DM